Mon. Not. R. Astron. Soc. **000**, () Printed 24 July 2007 (MN LATEX style file v2.2)

The SCUBA HAlf Degree Extragalactic Survey (SHADES) – IV: Radio-mm-FIR photometric redshifts

Itziar Aretxaga[1], David H. Hughes[1], Kristen Coppin[2,3], Angela M.J. Mortier[4,5], Jeff Wagg[6,1], James S. Dunlop[4], Edward L. Chapin[3], Stephen A. Eales[7], Enrique Gaztañaga[8,1], Mark Halpern[3], Rob J. Ivison[9], Eelco van Kampen[10], Douglas Scott[3], Stephen Serjeant[11], Ian Smail[2], Thomas Babbedge[12], Andrew J. Benson[13], Scott Chapman[13], David L. Clements[12], Loretta Dunne[14], Simon Dye[7], Duncan Farrah[15], Matt J. Jarvis[16,17], Robert G. Mann[4], Alexandra Pope[3], Robert Priddey[18], Steve Rawlings[17], Marc Seigar[19], Laura Silva[20], Chris Simpson[21], and Mattia Vaccari[22,12].

[1] *Instituto Nacional de Astrofísica, Óptica y Electrónica (INAOE), Aptdo. Postal 51 y 216, 72000 Puebla, Pue., Mexico*
[2] *Institute for Computational Cosmology, Durham University, South Road, Durham DH1 3LE, UK*
[3] *Department of Physics & Astronomy, University of British Columbia, 6224 Agricultural Road, Vancouver, B.C., V6T 1Z1, Canada*
[4] *SUPA (Scottish Universities Physics Alliance), Institute for Astronomy, University of Edinburgh, Blackford Hill, Edinburgh, EH9 3HJ, UK*
[5] *Center for Astrophysics and Planetary Science, School of Physical Sciences, University of Kent, Canterbury CT2 7NR, UK*
[6] *National Radio Astronomy Observatory, P.O. Box O, Socorro, NM 87801, USA*
[7] *Cardiff School of Physics and Astronomy, Cardiff University 5, The Parade, Cardiff, CF24 3YB, UK*
[8] *Institut d'Estudis Espacials de Catalunya, IEEC/CSIC, c/ Gran Capità 2-4, 08034 Barcelona, Spain*
[9] *UK ATC, Royal Observatory, Blackford Hill, Edinburgh, EH9 3HJ, UK*
[10] *Institute for Astrophysics, University of Innsbruck, Technikerstr. 25, A-6020, Innsbrusk, Austria.*
[11] *Astrophysics Group, Department of Physics, The Open University, Milton Keynes, MK7 6AA, UK*
[12] *Astrophysics Group, Blackett Laboratory, Imperial College, Prince Consort Rd., London SW7 2BW, UK*
[13] *Caltech, 1200 E. California Blvd., Pasadena, CA 91125-0001, USA*
[14] *The School of Physics and Astronomy, University of Nottingham, University Park, Nottingham, NG7 2RD, UK*
[15] *Department of Astronomy, Cornell University, Space Sciences Building, Ithaca, NY 14853, USA*
[16] *Centre for Astrophysics Research, Science & Technology Research Institute, University of Hertfordshire, Hatfield, AL10 9AB, UK*
[17] *Department of Astrophysics, Denys Wilkinson Building, Keble Road, Oxford, OX1 3RH, UK*
[18] *Department of Physics, Astronomy & Mathematics, University of Herdfordshire, College Lane, Hatfield, Hertfordshire AL10 9AB, UK*
[19] *Center for Cosmology, Dept. of Physics & Astronomy, Univ. of California, Irvine, 4129 Frederick Reines Hall, Irvine, CA 92697-4575, USA*
[20] *Osservatorio Astronomico di Trieste, Via Tiepolo 11, I-341311, Trieste, Italy*
[21] *Astrophysics Research Institute, Liverpool John Moores University, Twelve Quays House, Egerton Wharf, Birkenhead CH41 1LD, UK*
[22] *Department of Astronomy, University of Padova, Vicolo dell'Osservatorio 2, I-35122, Padova, Italy*

ABSTRACT

We present the redshift distribution of the SHADES galaxy population based on the rest-frame radio-mm-FIR colours of 120 robustly detected 850μm sources in the Lockman Hole East (LH) and Subaru XMM-Newton Deep Field (SXDF). The redshift distribution derived from the full SED information is shown to be narrower than that determined from the radio–submm spectral index, as more photometric bands contribute to a higher redshift accuracy. The redshift distribution of sources derived from at least two photometric bands peaks at $z \approx 2.4$ and has a near-Gaussian distribution, with 50 per cent (interquartile range) of sources at $z = 1.8 - 3.1$. We find a statistically-significant difference between the measured redshift distributions in the two fields; the SXDF peaking at a slightly lower redshift (median $z \approx 2.2$) than the LH (median $z \approx 2.7$), which we attribute to the noise-properties of the radio observations. We demonstrate however that there could also be field-to-field variations that are consistent with the measured differences in the redshift distributions, and hence, that the incomplete area observed by SHADES with SCUBA, despite being the largest sub-mm survey to date, may still be too small to fully characterize the bright sub-mm galaxy population. Finally we present a brief comparison with the predicted, or assumed, redshift distributions of sub-mm galaxy formation and evolution models, and we derive the contribution of these SHADES sources and the general sub-mm galaxy population to the star formation-rate density at different epochs.

Key words: surveys – galaxies: evolution – cosmology: miscellaneous – infrared: galaxies – submillimetre

1 INTRODUCTION

The SCUBA HAlf Degree Survey (SHADES, Dunlop 2005, Mortier et al. 2005) was originally designed with the aim of characterizing the star-formation history (Hughes et al. 2002) and clustering properties (van Kampen et al. 2005) of the bright-end of the luminous dust-enshrouded galaxy population. To achieve these goals we mapped two regions of the sky centered on the Lockman Hole East (LH) and Subaru XMM-Newton Deep Field (SXDF) with the Submillimetre Common-User Bolometer Array (SCUBA, Holland et al. 1999). With a proposed 1σ sensitivity of 2 mJy at 850μm the complete survey was predicted to identify a statistically robust sample of ~ 200 galaxies, with sufficient radio to FIR ancillary data to help identify optical/IR counterparts and derive spectroscopic/photometric redshifts. This redshift information is essential for determining the star formation and clustering properties for the whole population of ultraluminous dust-enshrouded galaxies. SCUBA was decommissioned in mid-2005 having covered ~ 40 per cent of the originally-proposed area of the SHADES[1].

Paper I of this series (Mortier et al. 2005) describes the survey motivation, strategy and the philosophy adopted for the analysis. Paper II (Coppin et al. 2006) presents the catalogue and number counts derived from the 850μm sources. Paper III (Ivison et al. 2007) describes the identification of radio and mid-IR counterparts of these sources. This paper (IV) constructs the redshift distribution derived from the radio-mm-FIR photometry of the SHADES sources based on a compilation of the 850μm and 450μm SCUBA data (Coppin et al. 2006), 1.4GHz Very Large Array photometry (Ivison et al. 2007) and other previously published mm to FIR photometric observations towards these fields. A study of the mid-IR to optical properties of the SHADES population, and further constraints on the photometric redshifts of the sources, will be published elsewhere (Clements et al. 2007, Dye et al. 2007, Serjeant et al. 2007). A spectroscopic study of a sub-sample of SHADES sources with identified optical/IR counterparts (Blain et al. 2007) will also provide an important comparison of spectroscopic and photometric redshifts.

The cosmological parameters adopted throughout this paper are $H_0 = 71\ \mathrm{km\,s^{-1}\,Mpc^{-1}}$, $\Omega_\mathrm{M} = 0.27$, $\Omega_\Lambda = 0.73$.

2 PHOTOMETRIC REDSHIFTS

Despite having mapped only ~ 40 per cent of the planned 0.5 sq. degree area, SHADES remains the largest extragalactic sub-mm survey to date. The difficulties of following-up such large areas at other wavelengths, and hence the inhomogeneity of the multi-wavelength data, implies that the same photometric redshift technique cannot be applied to all sources. This section has been divided in two subsections: the first (§ 2.1) deals with the consideration of 850μm and 1.4GHz photometry which is available for all sources, and the use of the sub-mm–radio spectral-index as a diagnostic of redshift; and the second (§ 2.2) describes the inclusion of additional photometry at 70 to 450μm which is sufficiently sensitive to place important constraints on the radio-mm-FIR photometric redshifts for only a few tens of sources. In both subsections we make a brief introduction to the techniques used, the estimated uncertainties found when comparing photometric and spectroscopic redshifts for similar sub-mm galaxies, the results from the application of the techniques to individual SHADES sources, and the combined redshift distributions derived for the entire SHADES population.

2.1 1.4GHz/850μm spectral index

2.1.1 Techniques and accuracies

One of the simplest redshift-indicators for the sub-mm galaxy population is that formed by the ratio of the flux densities at 1.4GHz and 850μm. These wavebands trace the tight correlation between radio continuum emission, which is dominated by synchrotron radiation from supernova remnants, and thermal emission from warm dust heated by young stars (Helou, Soifer & Rowan-Robinson 1985, Condon 1992, Yun, Reddy & Condon 2001). This redshift indicator was systematically studied by Carilli & Yun (1999, 2000), and has been subsequently revised for different sub-mm galaxy sub-populations (Dunne, Clements & Eales 2000, Rengarajan & Takeuchi 2001). The 1.4GHz to 850μm flux-density ratio, or a spectral index derived from it, increases monotonically with redshift, with some degeneracy due to the variety of radio synchrotron-slopes and mm dust-emissivity indices present in the ISM of those local galaxies used to define the relationship. Additionally there exists a level of degeneracy between the temperature of the dust generating the rest-frame FIR luminosity (and hence sub-mm flux) and the redshift. Regardless, by adopting a library of local galaxy templates, and accepting the intrinsic dispersion in their SEDs, the 1.4GHz to 850μm flux-density ratio still provides a crude but useful estimation of the redshift. This indicator becomes relatively insensitive to redshift beyond $z \sim 3$, as the 850μm filter starts to sample the flattening of the spectral energy distribution (SED) towards the rest-frame FIR peak, whilst still providing a powerful discriminant between low-redshift ($z < 2$) and high-redshift ($z > 2$) objects.

We shall discuss the 1.4GHz/850μm spectral index following two different prescriptions: (a) the single-template maximum-likelihood technique originally designed by Carilli & Yun (1999, 2000), denoted as $z_\mathrm{phot}^\mathrm{CY}$; and (b) a maximum likelihood technique which simultaneously fits the 20 local templates of starbursts, ULIRGs and AGN used by Aretxaga et al. (2003, 2005), denoted as $z_\mathrm{phot}^\mathrm{A}$.

The success of any photometric-redshift technique is measured by the accuracy with which it can predict the individual redshifts for a sample of representative galaxies with known redshifts, which have not been used to define the method. Aretxaga, Hughes & Dunlop (2006) have previously assessed the accuracy of the above two 1.4GHz/850μm photometric redshift indicators. Based on this study, we show in figure 1 a comparison of spectroscopic and photometric-

[1] The complete 1800 sq. arcmins SHADES area towards the LH and the SXDF has recently been surveyed at the JCMT at 1.1mm with AzTEC (Wilson et al. 2004), a continuum camera destined for the 50-m Large Millimetre Telescope (Serrano et al. 2006). These AzTEC data are currently being analysed and the results will be presented elsewhere.

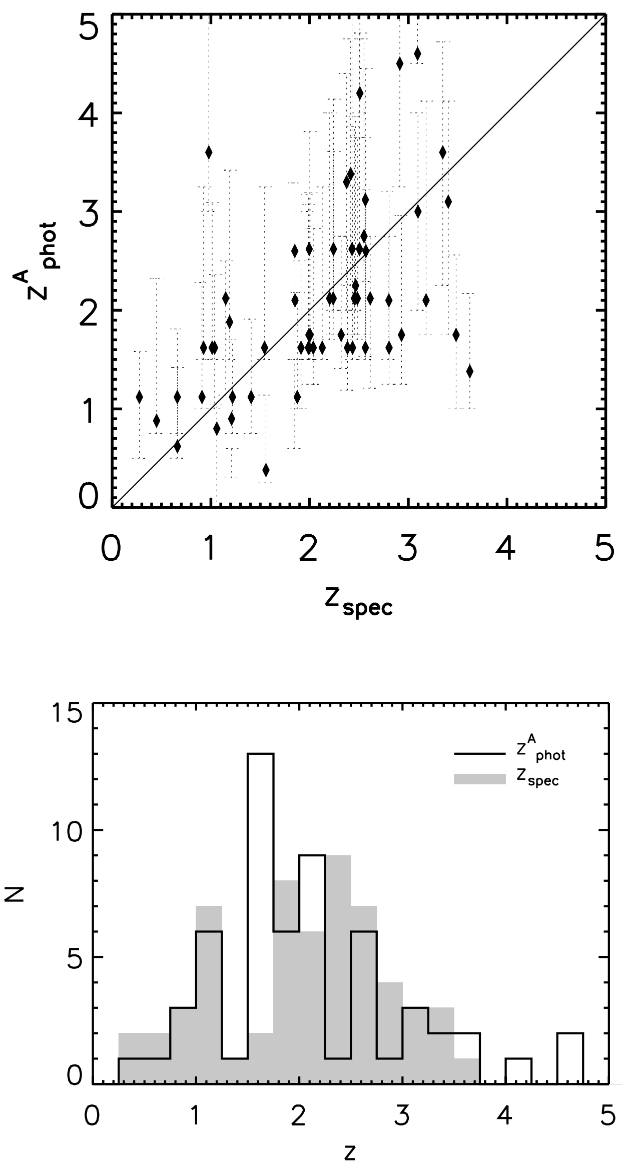

Figure 1. (Top) Comparison of spectroscopic and photometric redshifts derived from the 1.4GHz/850μm spectral index for a sample of 58 sub-mm galaxies with undisputed radio/optical/IR identifications, and spectroscopic redshifts derived from 2 or more lines (Aretxaga et al. 2006). The error bars represent 68% confidence intervals in the determination of the redshift. The r.m.s. scatter of the relation $z_{\rm spec} - z^{\rm A}_{\rm phot}$displayed is 0.8. **(Bottom)** Histogram distribution of the spectroscopic and photometric redshifts represented in the top panel, which illustrates the success in recovering the redshift distribution of the sample.

redshifts for 58 sub-mm/mm selected galaxies, complemented with a few objects selected at optical/FIR wavelengths, which have published optical/IR or CO spectroscopic redshifts and accompanying radio-FIR photometry. We will refer to this dataset as the 'comparison sample' hereafter. This comparison study shows that the $z^{\rm A}_{\rm phot}$ prescription has a mean accuracy $\Delta z \equiv < |z^{\rm A}_{\rm phot} - z_{\rm spec}| > \approx 0.65$ over the whole redshift interval, when one selects a robust sub-sample of objects with unambiguous optical/IR/radio counterparts and spectroscopic redshifts derived from the identification of two or more spectral lines. For the same robust sample of objects, $z^{\rm CY}_{\rm phot}$ has systematically larger errors, $\Delta z \approx 0.9$. This sample does not include powerful radio-loud AGN, for which the template SEDs used in the photometric redshift analysis are not appropriate. The r.m.s. of the relation is $< (z^{\rm A}_{\rm phot} - z_{\rm spec})^2 >^{1/2} \approx 0.8$. Restricting the analysis only to those galaxies with CO spectroscopic redshifts, the measured accuracy is $\Delta z \approx 0.6$ and has an r.m.s of 0.8 at $0 \leqslant z \leqslant 4$. The precision degrades as the redshift increases, as expected from the 1.4GHz/850μm spectral index, which flattens beyond $z = 3$ (Carilli & Yun 2000), leading to a measured $\Delta z \approx 1.0$ at $3 \leqslant z \leqslant 4$. Using all objects with published photometry and spectroscopic redshifts, regardless of whether the associations that lead to the spectroscopic redshift are unambiguous or not, the overall accuracy over the $0 \leqslant z \leqslant 4$ regime degrades to $\Delta z \approx 0.8$ (see Aretxaga et al. 2006, figure 1).

2.1.2 The redshifts of SHADES sources

The radio counterparts adopted for the photometric redshift calculations of SHADES sources are the secure sample detected within 8 arcsecs of the sub-mm position (Ivison et al. 2007), with a chance-association probability between the radio and sub-mm source of $P < 0.05$. We have accepted some additional counterparts when a robustly-detected radio source is still within 10 arcsec of the sub-mm centroid and, additionally, a 24μm counterpart is associated with this radio identification. These extra radio counterparts are marked in the notes provided for each sub-mm source (see tables 1 and 2), where we have calculated the corresponding P-value of the radio association, which remains lower than 0.08. The 34 radio sources adopted as counterparts of SHADES galaxies in the LH field, and the 35 radio sources in the SXDF have a combined chance association $P \approx 1.6$, and thus we expect to have incorrectly associated ~ 1 of the SHADES sub-mm sources with a projected radio source.

For both techniques the error bars of the photometric redshifts were derived by bootstrapping on the reported photometric and calibration errors (Coppin et al. 2006, Ivison et al. 2007), and are defined as the 68% confidence interval of the resulting redshift probability distribution. The photometric error distributions used for the 850μm photometry were derived by de-boosting the measured flux densities of the SCUBA sources. A de-boosting correction is necessary to provide a more accurate estimate of the flux of low S/N blank-field sources in sub-mm surveys, where the counts are typically very steep and faint galaxies can be statistically boosted above the nominal detection threshold. These errors are often non-Gaussian (see figure 5 in Coppin et al 2006). The 1.4GHz flux densities do not need to be de-boosted, since this correction is dependent on the area defined by the search radius in identifying the source. In the case of finding associations within $\lesssim 8$ arcsec radius around a known object, this is negligible. The error distributions for the 1.4GHz flux densities were assumed to be Gaussian. In the case of $z^{\rm CY}_{\rm phot}$, the error estimated by Carilli & Yun (2000), to allow for a difference in templates, is added in quadrature to the errors derived by bootstrapping the photometry.

The probability distribution calculated for each source

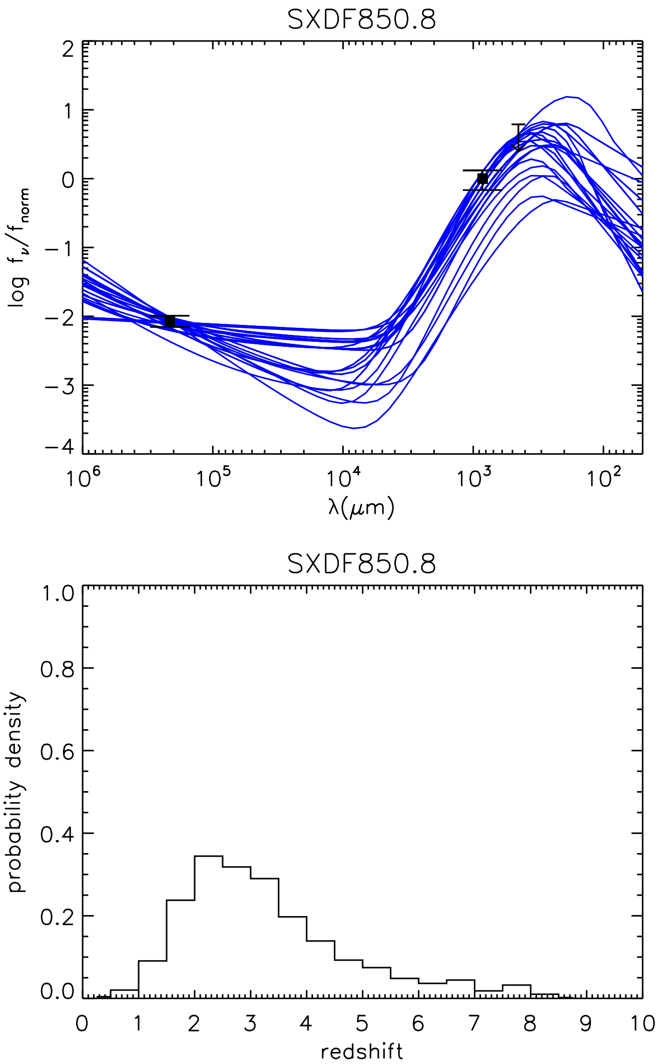

Figure 2. **(Top)** Spectral energy distribution (SED) of SXDF850.8, where the black squares mark the detections at 850μm and 1.4GHz used in the photometric redshift calculation. Error bars are 1σ, and the arrow at 450μm marks the 3σ upper limit derived from our maps. For reference, the SED templates used in the photometric redshift calculation are shifted to $z^{\rm A}_{\rm phot}$ = 2.6 and scaled to maximize the likelihood function of detections and upper limit through survival analysis (Isobe, Feigelson & Nelson 1986), and are represented as lines. All the SEDs are compatible within the 3σ error-bars of the photometry of the source. **(Bottom)** Probability distribution for SXDF850.8 derived for the $z^{\rm A}_{\rm phot}$ solution, using only the 850μm and 1.4GHz photometry.

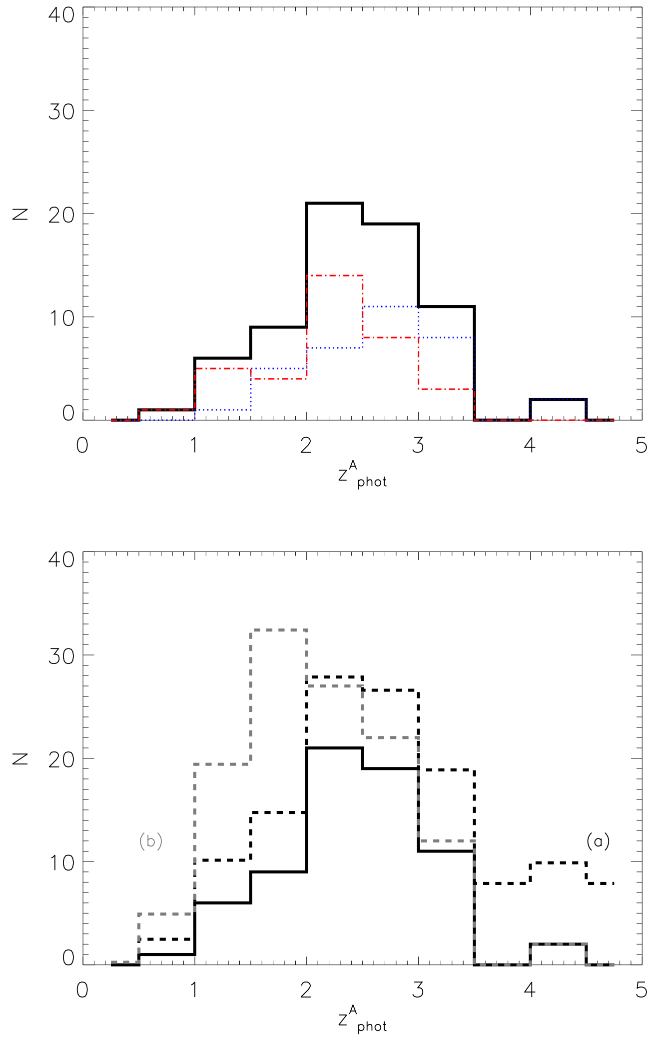

Figure 3. Histogram of modes of the photometric redshift distributions of SHADES galaxies derived from the 1.4GHz/850μm spectral index. The (black) thick solid-line (shown in the upper and lower-panels) represents the distribution of modes for the 69 galaxies that have been detected at both 850μm and 1.4GHz. In the upper-panel the (blue) thin dotted-line and (red) thin dash-dotted line represent the redshift distributions in the LH and SXDF fields respectively. In the lower-panel the black dashed-line (a) and grey dashed-line (b) show the redshift distributions for the full SHADES catalogue, including the 51 sub-mm galaxies undetected at 1.4GHz. Those SCUBA galaxies with non-detections in the radio are distributed in one of two ways that bracket the range of reasonable options: (a) with equal probability between their calculated lower 90% confidence limits and z = 5; and alternatively, (b) between their lower limits and z = 2, or only at their lower redshift-limits in the cases that these lie at $z > 2$.

in this manner typically have a single peak, which broadens as the most probable redshift of the source increases. Figure 2 shows an example of a typical solution derived from the use of 850μm and 1.4GHz photometry.

2.1.3 Redshift distribution of the SHADES population

We have assembled the best estimates of photometric redshift for each source in the LH and SXDF SHADES fields (figure 3). These are identified by the modes of the individual probability distributions, $z^{\rm A}_{\rm phot}$, which, by definition, are the redshifts with the highest probability values.

The galaxies that are not detected with confidence at radio-wavelengths, *i.e.* 26 out of the 60 galaxies in the LH, and 25 out of the 60 in the SXDF, have very flat individual redshift probability distributions in our computations, and hence we quote only the lower-limits to their redshift, which are defined as their 90% lower confidence-limits (tables 1 and 2). We incorporate these objects into the population distribution by adding flat probability distributions between their calculated lower 90% confidence limits and $z = 5$, and alternatively between their calculated lower 90% confidence limits and $z = 2$, or only at their lower redshift-limits if these indicate $z > 2$. These two alternative priors illustrate how the resulting redshift distributions (that include SHADES galaxies without radio detections) can be biased high and low.

Figure 3 shows the final photometric redshift distribution using the 1.4GHz/850μm spectral index, both for the full SHADES sample and for the LH and SXDF fields separately. The redshift distribution of SXDF sources peaks at slightly lower redshifts (median $z \approx 2.2$) compared to the distribution of LH sources (median $z \approx 2.6$). The low-redshift tail ($z < 1.5$) is also slightly more prominent in the SXDF than in the LH (6 vs. 1 sources among the radio-detected sample). The difference in shape of the two distributions of radio-detected sources can be measured using the two-tailed Kolmogorov-Smirnov (K-S) test, which gives a 3 per-cent chance that they are drawn from the same parent distribution. Furthermore, the mean-redshifts of the two distributions are significantly different at the 99.7 per cent level, according to a Mann-Whitney U-test. This difference can be attributed to differences in the noise levels of the radio maps, although some intrinsic variations between the fields are expected (see § 3).

For those objects with more than one redshift estimate (due to the ambiguity in their counterparts), we have produced alternative population distributions, with or without their inclusion, and with different combinations of possible counterparts. The results do not significantly change the final combined distribution. All figures presented in this paper include the primary radio association if there are multiple options.

2.2 Radio-mm-FIR SED analysis

The SHADES fields have been targeted by other FIR/sub-mm/mm and radio surveys. In this subsection we describe the extra constraints on the photometric redshifts that can be derived from these additional complementary data for a few tens of SHADES sources.

2.2.1 Techniques and accuracies

Photometric redshifts with modest precisions ($\Delta z \approx$ 0.3 to 0.5) have been obtained in the past few years using a combination of spectral indices between the radio and mm-wavelength regimes and the FIR spectral peak. This information has been exploited by several groups using a wide array of fitting-techniques and SEDs (e.g. Yun & Carilli 2002, Hughes et al. 2002, Aretxaga et al. 2003, 2005, Wiklind 2003, Hunt & Maiolino 2005, Laurent et al. 2006). There remain, however, degeneracies imposed by the choice of multiple SED templates, with FIR emission peaks distributed over a range of wavelengths, which can limit the precision of the derived redshifts (e.g. Blain, Barnard & Chapman 2003). We have previously developed a radio–mm–FIR technique based on Monte-Carlo simulations, that take into account constraining prior information such as the number counts of sub-mm galaxies, the favoured luminosity/density evolution up to $z \approx 2$, and the lensing amplification of a certain field (Hughes et al. 2002, Aretxaga et al. 2003, 2005). We only offer a brief summary of this technique here. A catalogue of 60μm luminosities and redshifts for mock galaxies is generated from an evolutionary model for the 60μm luminosity function that fits the observed 850μm number-counts (e.g. luminosity evolution $\propto (1 + z)^3$ for $z \lesssim 2$, and no evolution at $z > 2$) and covers a simulated area of 10 sq. deg. Template SEDs are drawn at random, without regard to their intrinsic luminosity, from a library of 20 local starbursts, ULIRGs and AGN, to provide FIR–radio colours for the mock galaxies. The SEDs cover a wide-range of FIR luminosities ($9.0 < \log L_{\rm FIR}/L_\odot < 12.3$) and temperatures ($25 < T/K < 65$). The flux densities of the mock galaxies include both photometric and calibration errors, consistent with the quality of the observational data for each sub-mm galaxy detected in a particular survey. We reject from the catalogue those mock galaxies that do not respect the detection thresholds and upper-limits of the particular sub-mm galaxy under analysis. The redshift probability distribution of an individual sub-mm galaxy is then calculated as the normalized distribution of the redshifts of the mock galaxies in the reduced catalogue, weighted by the likelihood of identifying the colours and flux densities of each mock galaxy with those of the sub-mm galaxy in question. This technique will be denoted $z_{\rm phot}^{\rm MC}$ in the discussion that follows.

The validity of the results derived from this technique is limited by the assumption that the SEDs of high-z sub-mm galaxies are similar to the local analogues, adopted as templates, which are scaled in luminosity and shifted in redshift. While this might seem a naive approach, all the templates used in the calculations that follow offer a good description of the radio–mm–FIR photometry of SCUBA galaxies, including 350μm observations (Laurent et al. 2006, Kovács et al 2006), with known spectroscopic redshifts and un-ambiguous multi-wavelength counterparts (Aretxaga et al. 2005). There are however a few sub-mm galaxies which do not match any of the templates we use in this paper at their published redshifts (see figure 4 in Aretxaga et al. 2006). In these examples their radio emission is higher than that implied by the radio–FIR correlation, possibly due to accretion activity, or their FIR emission peaks at wavelengths longer than those of the templates used in this study at the adopted redshift. We describe the redshift solutions for these galaxies as 'catastrophic' and this might be indicative of incompleteness in the library of SED templates used as analogues. There is still sufficient debate in the literature, however, about the nature and/or the ambiguity of the multi-wavelength counterparts to these sub-mm sources, from which the redshifts are derived, to justify their exclusion from a robust comparison sample (see Aretxaga et al. 2005, 2006, Laurent et al. 2006, Kovács et al. 2006 for a detailed complementary discussion on these galaxies).

In order to estimate the accuracy of the $z_{\rm phot}^{\rm MC}$ technique we use the full SED information of a robust sub-sample of 11 sub-mm galaxies, out of the comparison sample of 58 galaxies considered in §2.1.1, which have detections in three or more bands. Furthermore, the same galaxies have undisputed identifications of their optical/IR/radio counterparts and spectroscopic redshifts derived from the measurement of two or more spectral lines. We derive a mean accuracy

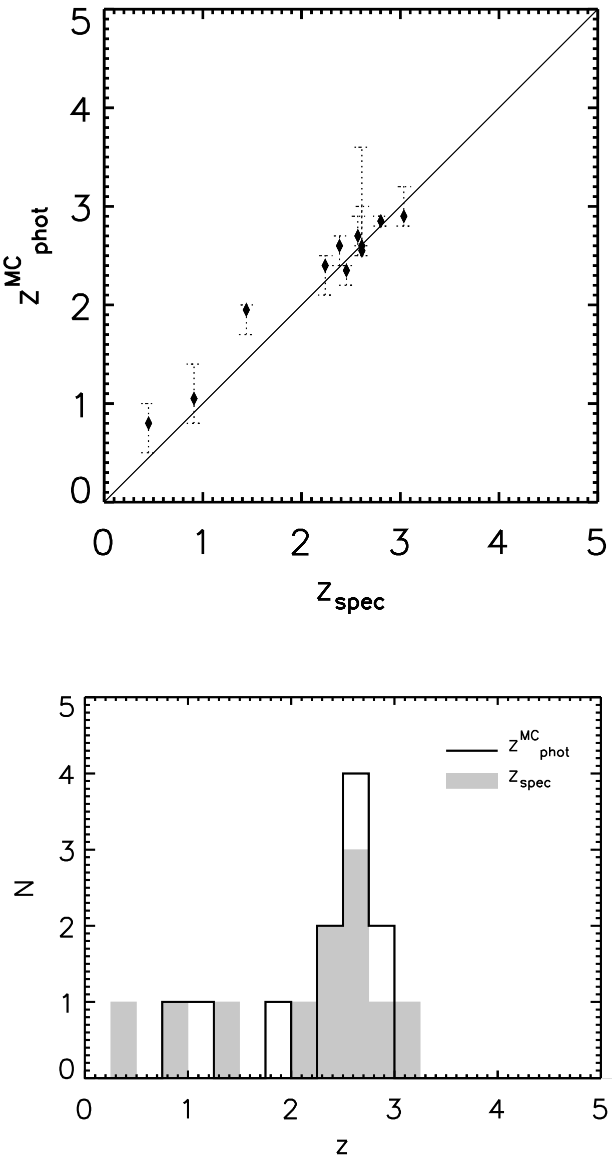

Figure 4. (Top) Comparison of spectroscopic and photometric redshifts derived from the full radio-FIR SED for a sample of 11 sub-mm galaxies with at least 3 robust detections at different wavelengths. This sample has undisputed radio/optical/IR counterparts associated with the sub-mm galaxies, and spectroscopic redshifts derived from 2 or more lines. The relationship has an r.m.s. of 0.25. **(Bottom)** Comparison of the distributions of the spectroscopic and photometric redshifts represented in the top panel.

for this sub-sample of $\Delta z \equiv < |z^{\rm MC}_{\rm phot} - z_{\rm spec}| > \approx 0.2$ and an r.m.s. $< (z^{\rm MC}_{\rm phot} - z_{\rm spec})^2 >^{1/2} \approx 0.25$ over the whole redshift interval (figure 4). Using all objects with published photometry, regardless of whether the spectroscopic redshift derived from the optical associations is ambiguous or not, the overall accuracy over the $0 \leqslant z \leqslant 4$ regime degrades to $\Delta z \approx 0.55$, with an r.m.s. of 0.80 (see figure 3 in Aretxaga et al. 2006). A few significant outliers which remain in the correlation are discussed by Aretxaga et al. (2005) and Kovács et al. (2006). Within the small sub-sample of study, the accuracy is independent of redshift.

If we restrict the use of photometry to 450μm upper limits combined with the 1.4GHz and 850μm detections for the comparison sample of galaxies (adopting simulated 450μm upper limits, when necessary, to mimic a shallower survey at this wavelength), we find a mean accuracy of $\Delta z \approx 0.55$ and an r.m.s. of 0.7 for the robust sample. This result is especially relevant for the photometric redshift calculations of the SHADES sources in §2.2.2, the majority of which have similarly sparsely-sampled photometry. Considering only the complete sample with robust and tentative spectroscopic redshifts the mean accuracy degrades slightly to $\Delta z \approx 0.65$, and the r.m.s. scatter is 0.90.

2.2.2 The redshifts of SHADES sources

Table 3 summarizes the most recent photometric redshifts calculated with the Monte Carlo technique for SHADES sources with additional photometry published in the literature. In contrast, and for completeness, tables 4 and 5 list the photometric redshifts derived only from the combination of the SHADES 450/850μm and the 1.4GHz photometry using two approaches: the Monte Carlo based technique, $z^{\rm MC}_{\rm phot}$ described above, and a non-prior maximum likelihood fit to the same 20 SEDs used for the first method that includes survival analysis (Isobe, Feigelson & Nelson 1986) to incorporate the non-detections into the maximum likelihood formalism, $z^{\rm SA}_{\rm phot}$. This second technique is introduced to provide a comparison of how the priors affect the redshift estimation of the sources and the final combined redshift distribution of SHADES galaxies. While most of the photometric redshifts derived from the two methods are similar, the pure survival analysis produces a few high-z catastrophic results in the robust comparison sample (2 out of 11). The overall reliability of the maximum likelihood technique is $\Delta z \approx 0.7$. These high-z catastrophic solutions get suppressed by the MC technique due to the weighting priors that disfavour high-z solutions for these sources, since, if they were typical of the sub-mm population, they would overproduce the 850μm number counts under the assumed luminosity evolution model. Although we give the values of photometric redshifts with and without priors in tables 4 and 5, we will now continue the analysis of the complete SHADES sample using only the MC solutions, since they have been shown to perform better against the comparison sample.

For 5 sources in table 5, SXDF850.5, 21, 28, 77 and 119, we also include complementary photometry at 70 and 160μm from the Spitzer Legacy Survey SWIRE (Lonsdale et al. 2003, Surance et al. 2007) that are used to derive mid-IR counterparts to the SHADES sources (Clements et al. 2007). The remainder of the SHADES sources are not significantly detected ($\geqslant 4\sigma$) in the Spitzer catalogues, and the noise properties of the SWIRE maps, providing 3σ upper-limits of $\sim$23 mJy and 160 mJy at 70 and 160μm, respectively (Afonso-Luis et al. 2007), do not further constrain the photometric redshifts.

Figure 5 shows the single-peaked redshift probability distribution derived for one of the sources that have the most complete photometric data. Although the majority of the sources show similar probability distributions, there are

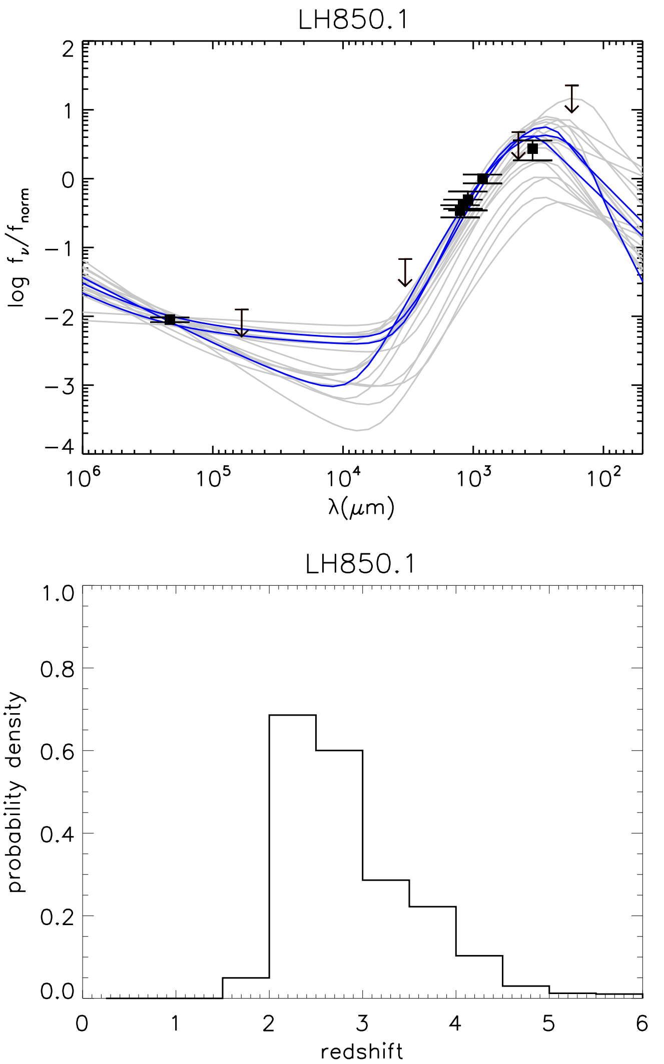

Figure 5. **(Top)** Spectral energy distribution (SED) of LH850.1, where the black squares mark detections, with 1σ error bars, and arrows indicate 3σ upper limits. For reference, the SED templates used in the photometric redshift calculation are shifted to $z_{\rm A}^{\rm MC} = 2.4$ and scaled to maximize the likelihood function of detections and upper limit through survival analysis (Isobe et al. 1986), and are represented as lines. The SEDs compatible within the 3σ error-bars of the photometry of the source are represented in darker (blue) lines. **(Bottom)** Probability distribution of LH850.1 derived for the $z_{\rm A}^{\rm MC}$ solution.

sometimes secondary peaks (see examples in Aretxaga et al. 2003). Nevertheless, it is always the primary redshift-peak that defines the solutions given in tables 3,4,5.

2.2.3 Redshift distribution of the SHADES population

Figure 6 shows our final photometrically-derived redshift distribution for the SHADES sources, using our best available estimate for the redshift of each source (i.e. $z_{\rm phot}^{\rm MC}$ taken from table 3 for those sources with the most complete photometry, and from tables 4 and 5 for the remainder)

The distribution of radio-identified SHADES sources clearly peaks in the bin $z \approx 2.0 - 2.5$, with a 50 per cent interquartile interval $z \sim 1.8 - 3.1$. We incorporate the non-radio detected sources (lower panel in figure 6) into the population distribution in two alternative ways, to serve as examples of how much these sources could alter the final population distribution: (a) approximating their individual probability distributions as flat distributions between their lower 90% confidence limit and $z = 5$; and (b) as flat distributions between their lower 90% confidence limit and $z = 2$, or at their lower limit if this lies at $z > 2$. Solution (a) is actually derived from the adopted non-informative (flat) prior for the photometric-redshift calculations. This creates a high-z tail which is a reflection of the adopted range for the flat redshift distributions which are unconstrained by the photometry. Solution (b) is biased against high-z, by imposing a maximum redshift for the radio-undetected sample which is lower than the redshift of the peak of the radio-detected sample. This radio-undetected sample could be composed of colder sub-mm galaxies than those found in the template library, or they could have the same template shapes as those adopted in the photometric redshift analysis, and still be undetected at the depth of the present radio surveys. Regardless, in these alternative solutions, the mode of the population remains at $z \approx 2.0 - 2.5$, with at least 50 per cent of the galaxies in the interquartile range $1.6 \leqslant z \leqslant 3.4$.

In order to consider the effect of the objects with more than one redshift estimate (due to ambiguity in their radio-counterparts), we have produced alternative population distributions. For instance, figure 6 shows the combination of the first entries for each source in tables 3, 4, 5. The introduction of the second tabulated values instead of the first ones, for those sources with ambiguous associated photometry, produces an alternative distribution which is indistinguishable (with a 99.96 per-cent probability), via a Kolmogorov-Smirnov (K-S) test, from the one represented here.

As in the case of the photometric redshift distribution derived from the 1.4GHz/850μm spectral index, the distribution of redshifts derived from the full SED analysis of SXDF sources peaks at slightly lower redshifts (median $z \approx 2.2$) than that of LH sources (median $z \approx 2.7$), and its low-redshift tail ($z < 1.5$) is also more prominent. These differences in the distributions are statistically-significant, as indicated by a K-S test at a level of 98.9%. A Mann-Whitney U-test shows that their mean-redshifts differ at the 99.997% level.

3 DISCUSSION

3.1 Redshift distribution

SHADES was designed with the objective of constraining the redshift distribution and clustering properties of the sub-mm galaxy population, an exercise which van Kampen et al. (2005) demonstrated could discriminate between galaxy formation models. With ∼40 per cent of the survey completed before SCUBA was de-commissioned in the summer 2005, SHADES has provided 120 robust sources. The radio-mm-FIR photometry assembled for the survey favours a nearly Gaussian redshift distribution of the population peaking at $z \approx 2.0{-}2.5$, albeit still with the possibility of a high-redshift tail remaining.

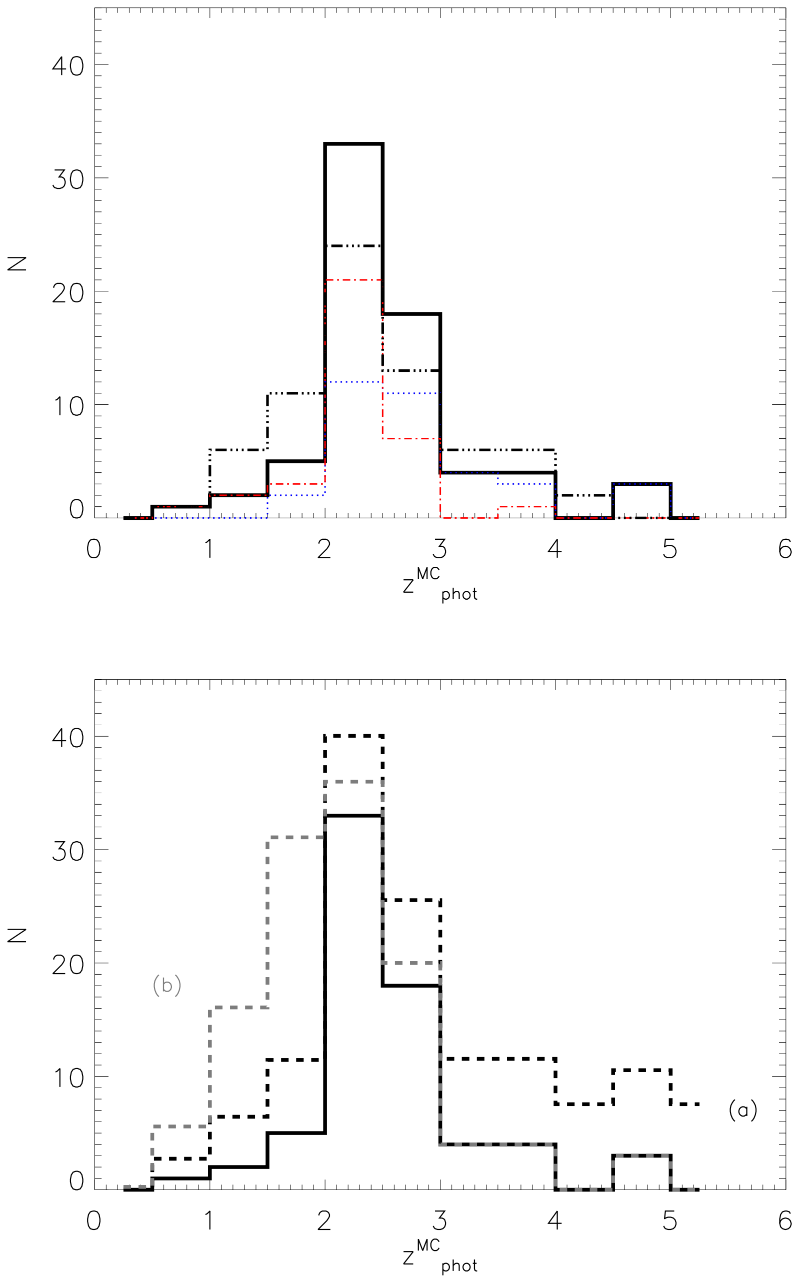

Figure 6. Histogram of the modes of the photometric redshifts of SHADES galaxies based on all available radio-mm-FIR photometry (provided in table 3, or otherwise in tables 4 and 5). **Upper Panel:** The thick solid-line (also shown in the lower-panel) represents the $z^{\rm MC}_{\rm phot}$ distribution of modes for those 70 SCUBA galaxies that have been detected in at least two bands, of which the thin (blue) dotted-line and thin (red) dash-dotted line represent the distributions defined by the LH and SXDF sources, respectively. For comparison, we plot the $z^{\rm SA}_{\rm phot}$ solutions for the full distribution of LH and SXDF (dash–3-dot line). **Lower Panel:** The black dashed-line (a) and grey dashed-line (b) show the redshift distributions for the 70 SCUBA galaxies detected in at least two bands, plus an additional 50 SCUBA galaxies detected only at 850μm. These latter sources are distributed in one of two ways that bracket the range of reasonable options: (a) with equal probability between their calculated lower 90% confidence limits and $z = 5$; and alternatively, (b) between their lower limits and $z = 2$, or only at their lower redshift-limits in the cases that these lie at $z > 2$.

The photometric redshift distribution of the radio-detected sub-mm galaxies is qualitatively similar to the optical spectroscopic redshift distribution published by Chapman et al. (2003, 2005) who followed-up a sample of sub-mm galaxies derived from various surveys. The agreement is perhaps not surprising, given that the photometric redshifts of the comparison sample have shown a relatively good agreement with the spectroscopic redshifts published in the literature (Aretxaga et al. 2006, §2.1.1, 2.2.1). Furthermore, the majority of the sub-mm sources that have spectroscopic redshifts are drawn from SCUBA surveys of similar depths to SHADES.

The high-redshift correction applied to the measured spectroscopic redshift distribution, suggested by Chapman et al. (2005) to account for the bias introduced by non-detection of the higher-redshift radio counterparts that provide candidates for optical spectroscopic follow-up, also falls within the range of photometric redshift estimations we have derived for SHADES sources that are not detected at radio-wavelengths. These sources provide the high-redshift ($z > 3$) tail of figure 6, and could in fact be placed anywhere above $z \sim 1.0$, even producing secondary peaks.

Our calculations do not support the existence of a substantial low-redshift ($z < 1.5$) tail within the luminous sub-mm radio-detected population sampled by SHADES. At first sight this might appear to be in conflict with the results of Pope et al. (2005, 2006) who found that $\sim 30\%$ of the sub-mm sources found in the SCUBA imaging of the GOODS-North field may lie at $z < 1.5$. If the GOODS-North 850μm catalogue is restricted to sources with de-boosted flux densities $S_{850} > 3$mJy, however, then the proportion of robustly identified sub-mm galaxies which lie at $z < 1.5$ drops to 6%. This is entirely consistent with the results found here for SHADES galaxies. Thus, these results may be providing further evidence that the peak of the redshift distribution of sub-mm sources is positively correlated with sub-mm flux-density/luminosity, consistent with the apparently anti-hierarchical nature of star-formation history reported in several other recent studies (e.g. Heavens et al. 2004). Furthermore field-to-field variations in the spatial distribution of the large-scale structure can provide a simple explanation for the differences between the redshift distributions of sub-mm sources derived from the individually-mapped contiguous-areas (typically < 0.2 sq. degrees) taken from the current generation of SCUBA surveys.

Our analysis also suggests that only a modest fraction of sub-mm galaxies could be hiding in the optical redshift-desert at $z \approx 1.5 - 1.8$ during spectroscopic searches for SHADES sources with robust radio counterparts. The photometric redshift probability density distributions of radio-detected SHADES sources using the 1.4GHz/850μm index or the full radio–mm–FIR SED information contain ~ 15 % and $\sim 10\%$ of sources in this redshift desert regime, respectively.

The difference between the redshift distribution of sub-mm sources in the SXDF and LH fields is entirely consistent with the different properties of the 1.4-GHz maps as discussed by Ivison et al. (2007). The LH data have a higher VLA resolution than those in SXDF, and the LH data are also deeper, although the coverage is less uniform. There is clearly potential for systematic differences between radio measurements in the LH and SXDF. For an extended source in the LH (of which there are several – Ivison et al. 2002), a larger fraction of emission on scales larger than the synthesized beam will be resolved away than for similar cases in SXDF. Moreover, the LH data will suffer greater significant bandwidth smearing and, although the appropriate correction has been made to the measured flux densities, some faint sources will be lost below the radio-detection threshold and may receive misleadingly low flux-density limits. These effects can be viewed as a systematic flux calibration offset with consequences as severe as those encountered in optical/infrared photometric-redshift estimation. While random 1.4GHz calibration uncertainties of 5 per cent have been accounted for in the estimation of the photometric redshifts, a systematic flux-density offset could shift the redshift distribution significantly. In order to explore this possibility, we have applied a 10 per cent flux increase to the LH photometry and recalculated the photometric redshifts. The combined redshift distribution shifts its peak by ~ -0.25, and consequently the mean values of the SXDF and LH distributions are more consistent, increasing from 0.3 per cent (§2.1.3) to a 7 per-cent probability, according to a Mann-Whitney U-test. Some intrinsic variation on the distribution of redshifts between the fields is however to be expected (see below).

3.1.1 Comparison of the SHADES redshift distribution with galaxy formation models

Van Kampen et al. (2005) studied four different galaxy formation models that yielded different redshift distributions and clustering properties for the sub-mm population expected to be found in a survey of the depth and area covered by SHADES: (α) a hydrodynamical model (Muanwong et al. 2002), that follows the evolution of dark-matter, gas, star-like particles and galaxy fragments, that has been coupled with the analytical form for redshift distribution of Baugh, Cole & Frenk (1996); (β) a simple merger model that identifies sub-mm galaxies with major mergers of massive galaxies; (γ) a phenomenological model (van Kampen 2004), which is based on N-body simulations that identify the sites of major-mergers and has two modes of star formation, quiescent and bursting; and (δ) a stable clustering model (Gaztañaga & Hughes 2001). Figure 7 represents the theoretical redshift distributions of SHADES galaxies found in these models. This figure has been complemented with (ϵ) a semi-analytical model for the joint formation and evolution of spheroids and QSOs (Granato et al. 2004, Silva et al. 2005); and (ζ) an alternative semi-analytic model of galaxy formation for sub-mm galaxies (Baugh et al. 2005).

Furthermore, to enable a more accurate discrimination between the above predictions, all the galaxy formation models in figure 7 account for the incompleteness of sources in the SHADES catalogue (Coppin et al. 2006). The models have also been convolved with a representative radio-mm-FIR photometric precision of $\sigma \sim 0.4$, which is intermediate between the measured uncertainties derived for the two techniques used in this paper.

We have made a comparison, via a K-S test, of the observed redshift probability density distributions with those predicted from the above models. In each case a K-S statistic has been calculated that accommodates the 1σ uncertainty in the median redshift of the models due to field-to-field variations. A study of 25 simulations made for each of the four models analyzed by van Kampen et al. (2005) demonstrate that the mean redshift of ~ 60 SHADES-like sub-mm galaxies varies by $\delta\bar{z}$ (r.m.s.) $\approx 0.25 - 0.55$. In part these shifts can be explained by Poisson noise (estimated $\sigma \sim 0.1 - 0.2$ from the simulations). The models show, however, that there could also be a significant component in the field-to-field variations that arises from intrinsic redshift differences due to varying amounts of groups or proto-clusters of galaxies along the line-of sight. Thus the differences found between

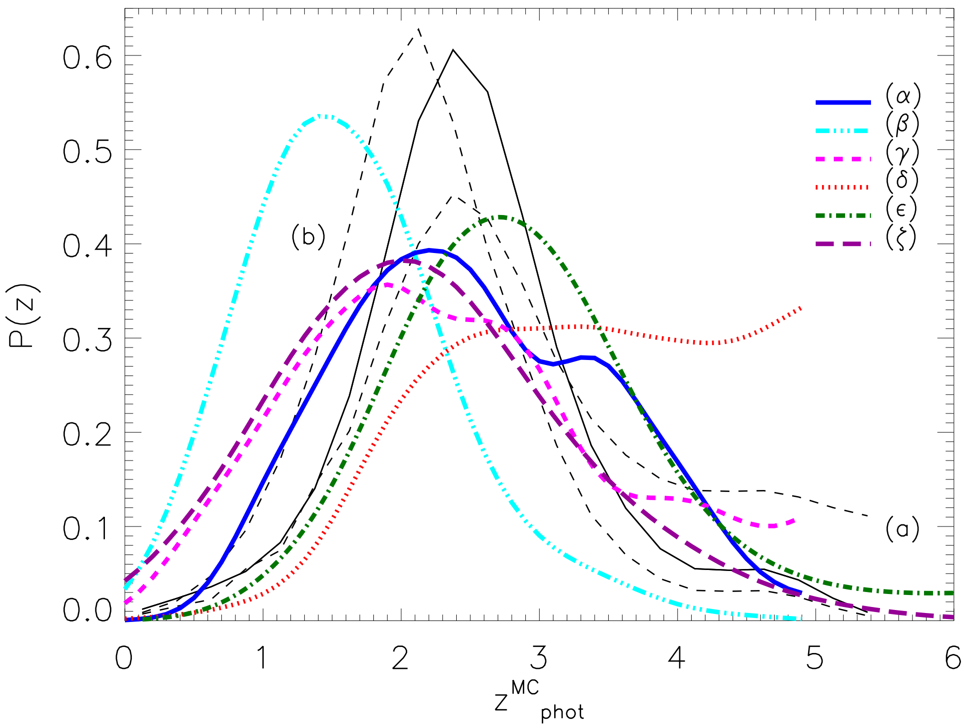

Figure 7. Probability density of the combined redshift distribution of SHADES galaxies (thin black solid-line, and thin dashed-lines ((a) and (b)), as described in figure 6). These are compared with the redshift distributions of six galaxy formation models (thick coloured-lines), degraded with a $\sigma_z = 0.4$ to provide representative redshift-uncertainties: (α) the hydrodynamical model of Muanwong et al. (2002) coupled with the analytical form for redshift distribution of Baugh, Cole & Frenk (1996); (β) the simple merger model of van Kampen et al. (2005); (γ) the phenomenological model of van Kampen (2004) and van Kampen et al. (2005); (δ) the stable clustering model of Gaztañaga & Hughes (2001); (ϵ) the semi-analytical model for the joint formation and evolution of spheroids and QSOs of Silva et al. (2005); and (ζ) the semi-analytic model for galaxy formation of Baugh et al. (2005).

the LH and SXDF areas, and between these and smaller, deeper surveys like GOODS-N, could be partially explained by this effect.

The results of the K-S test suggest that only model (ϵ) is close to being formally acceptable, with an 87% probability for the model to agree with the measured probability density distribution that includes SHADES sources with and without radio-detections according to solution (a). With only a small shift ($\delta z \sim -0.3$) in the distribution, model (ϵ) also qualitatively reproduces ($\sim$ 60% probability of similarity) the photometric-redshift distribution of the radio-detected SHADES galaxies.

The SHADES sources in our analysis that are not detected at radio wavelengths have very flat redshift probability distributions, which simply places them at $z \gtrsim 1.0$, and hence these SHADES sources could also produce a secondary peak in the redshift distribution. In the ranking of similarities of measured and model-distributions, models (α) and (γ), $\sim$ 45% probability, have double peaks and are broader than the observed distributions. A different prior, that optimizes the redshift-distribution of the SHADES sources without radio-detections, could bring them closer to a level of formal-acceptance. Finally models (δ), (ζ) and (β) are all rejected with probabilities of < 2% of being consistent with the range of solutions depicted in figure 7.

3.2 The FIR luminosity of SHADES sources

The catalogues of redshifts presented in tables 1 to 5 are an initial step towards characterizing the FIR luminosities and star formation rates of the SHADES population. The available photometry in the FIR peak regime (70–450μm), however, is not deep enough to fully constrain the SEDs of most SHADES sources at these wavelengths. One viable approach is to use the 20 SEDs in our local template catalogue to derive the corresponding FIR luminosities from the 850μm flux densities, bearing in mind that the lack of constraints at short wavelengths will dominate the errors in luminosity estimation over those of redshift (e.g. Hughes et al. 2002). Alternatively, one could use the 1.4GHz radio flux density to deduce FIR luminosities via the radio-FIR luminosity correlation that characterizes the sub-mm galaxy population, since this now has been extended to $z \sim 0.5-4$ (Kovács et al. 2006). This latter approach has the advantage of providing mean FIR luminosities which are accurate for the bulk of the population, reducing the uncertainties in luminosity primarily to the accuracy of the photometric redshifts. However, the normalization of the relation might be shifted from the local IRAS correlation, and this could affect the FIR luminosities derived, and the comparison of these to nearby galaxies.

Regardless of this complication, the observed 1.4GHz

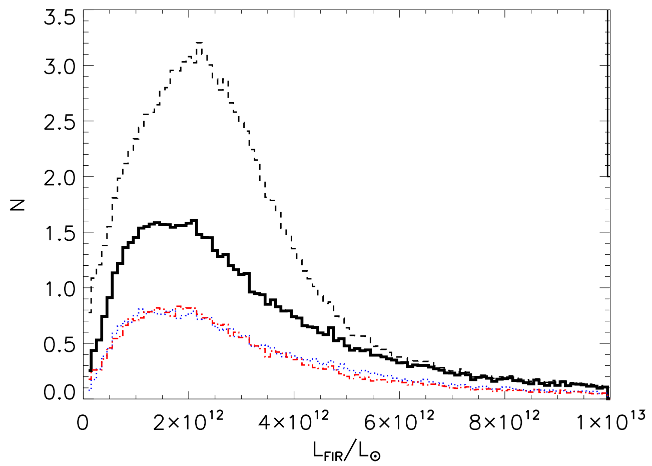

Figure 8. Distribution of FIR luminosities of the 120 SCUBA galaxies in the SHADES catalogue. The solid-line represents the total distribution of radio-detected sub-mm sources in the two fields towards the LH (thin blue dotted-line) and SXDF (thin red dashed-dotted line) based on the FIR-radio correlation of sub-mm galaxies (Kovács et al. 2006). The dashed line shows the complete distribution of FIR luminosities for all SHADES sources, including the 51 non-radio-detected sub-mm sources, where the FIR luminosities of the latter sources have been derived from a single $T = 35$K, $\beta = 1.5$ grey-body scaled to the observed 850μm flux density, and their redshifts have been selected at random between their lower 90%-confidence redshift-limits and, arbitrarily, $z = 5$.

flux densities have been converted to rest-frame 1.4GHz flux densities using a mean synchrotron radio slope of index $\alpha = -0.7$, and the monochromatic 1.4GHz luminosity has been inferred using the photometric redshift solution for each source. This is converted to FIR luminosity using the linear relationship $\log(L_{\rm FIR}/L_{1.4{\rm GHz}}/4.52\,{\rm THz}) = 2.14 \pm 0.07$ (Kovács et al. 2006). For each source we have considered the effect of the uncertainties in redshift, 1.4GHz flux and the reported scatter in the sub-mm galaxy FIR-radio correlation (Kovács et al. 2006) by bootstrapping 1000 times on the measured errors. For the 69 radio-detected SHADES sources in the LH and SXDF fields the median FIR luminosity is $2.6 \times 10^{12}{\rm L}_{\odot}$, with a high luminosity tail that extends to $1\times10^{13}{\rm L}_{\odot}$ (see figure 8). The distribution of luminosities for sources in both the LH and SXDF fields are similar.

The effect of non-radio-detected sources, which have very unconstrained and possibly high redshifts (§2.1), has also been considered by scaling a simple grey-body of temperature $T = 35$ K and emissivity index $\beta = 1.5$, the average of a parametrized SED of the short sub-mm wavelength detected SCUBA galaxies that define the radio-FIR correlation at $z \sim 1-3$ (Kovács et al. 2006), to the observed 850μm flux density. The errors in the 850μm flux density have been taken into account by bootstrapping on the inferred de-boosted distributions of 850μm flux densities for each source, and the redshift has been selected at random between their 90 per cent lower-limits (tables 4, 5) and, arbitrarily, $z = 5$. The resulting combined distribution has a median FIR luminosity of $2.6 \times 10^{12}{\rm L}_{\odot}$, the same as the distribution of radio-detected sources.

If one returns to the alternative approach of using the combination of 20 SEDs with the de-boosted 850μm flux densities to derive the FIR luminosities, one derives a broader luminosity distribution than that depicted in figure 8, reflecting the wide variety of acceptable SED templates, with a median luminosity that is increased by $\sim$ 40 per cent.

3.3 The star formation-rate history derived from SHADES galaxies

The evolution of the global star formation rate (SFR) density traced by SHADES sources is shown in figure 9. The conversion from FIR luminosity to star formation rate was performed using a constant of 5×10^{9} ${\rm L}_{\odot}/({\rm M}_{\odot}{\rm yr}^{-1})$, which is constrained to $\sim \pm30$ per cent uncertainty (Kennicutt 1998). We have multiplied the contribution of each source to the star formation density by the inverse of the SHADES survey completeness function at the appropriate flux density (Coppin et al. 2006). Redshift-space was binned into six intervals, and a Monte Carlo was performed to assign each galaxy to a redshift bin according to its expected photometric redshift error. The FIR luminosities have been estimated from the radio-FIR correlation or with a single SED which is considered to be representative of the sub-mm galaxy population (as in §3.2). The error bars in SFR density are the result of the uncertainties in photometry, SEDs and redshift, and are computed as the standard deviation traced by 1000 Monte Carlo simulations.

The evolution in the SFR density traced by the radio-detected sources shows a clear peak at $z \sim 2.5$ and a slow decline at both low and high redshifts. A good description of the SFR density traced by this population is given by $\dot{\rho}_{\rm SF} \approx 0.35\exp\left[-0.5(z-2.8)^2/(0.8^2)\right]$. The contribution of non-radio-detected SHADES sources to the SFR history may be significant at high-redshifts compared to the radio-detected SHADES sources, as indicated in figure 9 by the empty black diamonds (solution (a) in figure 6). Since the redshifts of these sources are not well constrained, this should be considered as only a possible evolutionary history, awaiting confirmation by better multi-wavelength data to improve the constraints on the redshifts of the radio-undetected SHADES sources. The effect of placing all the radio-undetected sources between their lower redshift-limits and $z = 2$ or at their lower limits if they are at $z > 2$ (solution (b) in figure 6) is shown by the grey empty diamonds in figure 9, which understandably broadens the peak of star formation density to lower-z.

The levels of star formation deduced for SHADES sources are consistent with those derived for other samples of radio-detected sub-mm galaxies at $z \leqslant 3.5$ (Chapman et al. 2005). At higher-redshifts, however, the SFR densities implied in this photometric-redshift study exceed the extrapolations of Chapman et al. Eventually spectroscopic measurements of SHADES sources at $z > 3.5$, via millimetre-wavelength observations of molecular CO-lines, or optical spectroscopy with increased sensitivity, will provide a definitive measurement of the SFR density of obscured galaxies in the high-redshift Universe.

In order to estimate the contribution to the global star formation rate density of 850μm sources that are fainter than those detected by SHADES, we have adopted the 60μm luminosity function with a pure luminosity evolution that

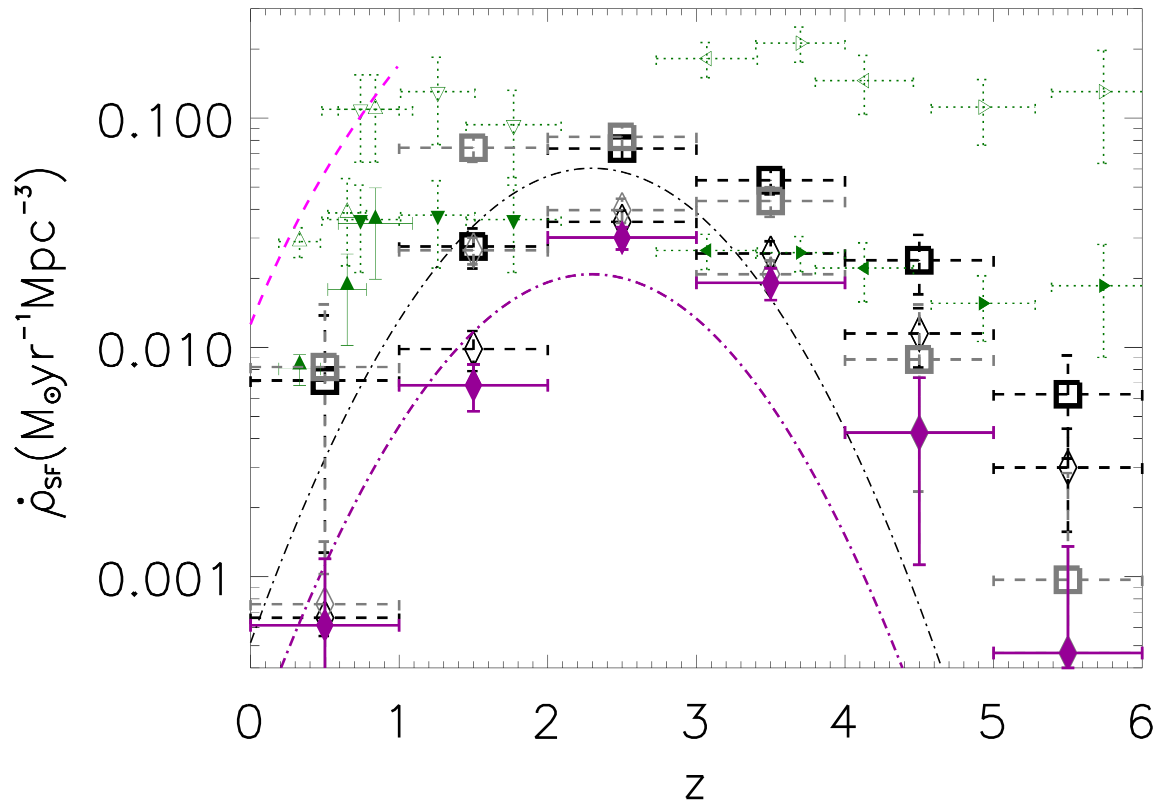

Figure 9. Evolution of the global star formation rate density (SFRD) for different samples of galaxies. We show the SFRD for radio-detected SHADES sources (solid diamonds) and for all SHADES galaxies, considering both the radio-detected and radio-undetected sources (open diamonds). The redshift probability distributions for the radio-undetected sources have been assumed to be flat between their lower redshift-limits (tables 4, 5) and $z = 2$ (grey open diamonds) and $z = 5$ (black open diamonds). The redshift error-bars indicate the width of the redshift bins. The error-bars in $\dot{\rho}_{\rm SF}$ are a combination of the uncertainty in the photometry, the recovery of the luminosity of each source due to SED differences, and the uncertainty in redshift that divides the contribution of sources across several redshift bins (see §3.3). The empty-square grey/black symbols represent the SFRD traced by ultraluminous 850μm-selected starbursts, by correcting the SFRDs derived for SHADES galaxies via the completion of the IRAS 60μm luminosity function with pure luminosity evolution up to $z = 2$ (§3.3). The (pink) dashed-line shows the SFRD inferred from 24μm-selected luminous and ultraluminous infrared galaxies (Le Floc'h et al. 2005), which follow a similar luminosity evolution to that presented here for the SHADES galaxies. The (purple) thick dash-dotted line shows the SFRD for the sample of SCUBA galaxies from Chapman et al. (2005). The thin dash-dotted line, which is a factor of ~ 3 higher, is an estimation of the contribution of 850μm-selected galaxies down to the ~ 1 mJy level. The SFRDs for optical/UV-selected starbursts are shown as small triangles, and are taken from Lilly et al. (1996 – upward-pointing triangles), Connolly et al. (1997 – downward-pointing), Steidel et al. (1999 – left-pointing) and Giavalisco et al. (2004 – right-pointing). The optical/UV data are shown with and without corrections for dust-obscuration as empty and solid triangles respectively, and all data have been homogenized to the same set of parameters and corrected to complete a Schechter luminosity-function (Giavalisco et al. 2004). All estimates have been converted to the same SFR/$L_{\rm IR}$ factor and cosmological model described in § 1.

follows $(1+z)^3$ at $z \leqslant 2$, and then maintains a constant level for $z > 2$. This evolutionary form provides an adequate description of the 850μm and 1.1mm counts (e.g. Scott et al. 2002, Greve et al. 2004) and is also supported up to $z = 1$ by the evolution of the luminosity function of 24μm–selected galaxies (Le Floc'h et al. 2005). By implementing this luminosity-function correction the SFR density increases up to a maximum factor of 2 at $z > 2$.

The contribution of SHADES galaxies to the global star formation rate density of the Universe is comparable to the contribution of starbursts selected at optical/UV wavelengths at $1 \lesssim z \lesssim 4$ before the latter are corrected for dust extinction. It is important to recall that the $L_{\rm FIR}$/SFR factor we have adopted could be in error by $\sim \pm 30$ per cent, and that SED differences could also account for an increase of ~ 40 per cent. These uncertainties have not been carried into the estimation of error-bars in figure 9. If we complete the luminosity function of SHADES galaxies towards lower luminosities, the FIR star formation rate traced by ultraluminous starbursts is still a factor of 1.2 to 2 lower than that of optical/UV starbursts that have been corrected for intrinsic dust extinction.

The recent demonstration that the contribution of luminous and ultraluminous IR galaxies dominates the SFR density at $z \leqslant 1$ (Le Floc'h et al. 2005) suggests that even if we correct for the incomplete sampling of the sub-mm galaxy luminosity function, a bright SHADES sub-mm survey could be missing the integrated contribution of dusty starbursts to the global SFR by a large factor (as high as ~ 7), and thus dusty starbursts could indeed prove to be a significant mode of the star formation of the Universe (Blain et al. 1999).

The contribution of the fainter (< 3 mJy) 850μm sub-mm galaxy population to the star formation history of the Universe at $z > 1$ remains unconstrained at present, since detecting faint sub-mm galaxies has been restricted to a few strongly-lensed fields (e.g. Smail, Ivison & Blain 1997) and extremely-deep confusion-limited pencil observations (e.g. Hughes et al. 1998). Our estimations presented in figure 9 should therefore be considered an educated estimate of how ultraluminous IR-submm galaxies trace the star formation history of the Universe.

Accurate measurements of the surface density and redshift distribution of the entire sub-mm galaxy population (and the faintest galaxies in particular) that contribute the complete sub-mm to FIR extragalactic background require deeper and larger mm and sub-mm surveys than are currently possible. The anticipated continuum and spectroscopic surveys with SCUBA-2 (Holland et al. 2006), the Large Millimetre Telescope (LMT, Serrano et al. 2006), and the Atacama Large Millimeter Array (ALMA, Beasley, Murowinski & Tarenghi 2006), for example, will provide suitable data. In the meantime, however, it is still possible that the redshift distribution of the more populous and fainter (possibly extremely high-redshift or alternatively less luminous) sub-mm galaxies is significantly different to those galaxies identified in the SHADES survey.

4 SUMMARY OF CONCLUSIONS

• We have derived the photometric redshift distribution of SHADES sources with de-boosted 850μm flux densities > 3 mJy towards the Lockman Hole (LH) and the Subaru/XMM Newton Deep Field (SXDF) using rest-frame radio to FIR photometry. The redshift distribution of the radio-detected sub-mm sources peaks at $z \sim 2.4$ with 50 per cent of the population between redshifts 1.8 and 3.1.

• The combined redshift distribution of SHADES sources with robust radio counterparts, ~ 60 per cent of the population, has a distribution which is qualitatively consistent with the distribution of rest-frame UV-optical spectroscopic redshifts published by Chapman et al. (2005).

• We find a small ($\delta z \approx 0.5$), but significant, difference between the peaks of the photometric-redshift distributions of the LH and SXDF, which can be attributed to differences in the sensitivities of their respective radio maps. Intrinsic field-to-field redshift variance is also expected, and is characterized according to a variety of models ($\delta z \approx 0.25 - 0.55$). This drives us to the conclusion that the incomplete area (~ 720 sq. arcmins) observed by SCUBA, despite being the largest sub-mm survey to date, may still be too small to be a representative sample of the bright sub-mm galaxy population.

• The complete redshift distribution of all SHADES sources, including those sub-mm sources without detections at radio wavelengths (for which we adopt a variety of possibilities that describe their unconstrained distribution of redshifts) still maintains the peak (mode) of the bright sub-mm galaxy redshift distribution at ≈ 2.4. We have considered a variety of priors that describe the unconstrained redshift distributions of the sub-mm sources without radio detections. In the most extreme solutions, distributing these sources with equal probability between their lower redshift-limit and $z = 2$ or $z = 5$, the bulk of the sub-mm population (50 per cent interquartile) lies in the range $1.6 \leqslant z \leqslant 2.6$ or $2.1 \leqslant z \leqslant 3.4$, respectively.

• The combined SHADES LH and SXDF redshift probability-density distribution is compatible, within the uncertainties of our analysis, with the semi-analytical model for the joint formation of spheroids and QSOs of Granato et al. (2004) and Silva et al. (2005). If sources detected only at 850μm are also introduced into the redshift probability-density, with other priors than those illustrated here, then the hydrodynamical model of Muanwong et al. (2002) and phenomenological model of van Kampen (2004) and van Kampen et al. (2005) could also be in agreement with the observations. These compatible models, which are physically quite distinct, predict different clustering properties for the SHADES galaxies that could allow further discrimination between them (van Kampen et al. 2005). A detailed study of the clustering properties of SHADES galaxies will be the topic of a further paper.

• The bright SHADES galaxies contribute to the SFR density of the Universe with ~ 0.01 to 0.03 M$_\odot$ yr^{-1} Mpc^{-3} in the redshift interval $1 \lesssim z \lesssim 5$, and reach the levels of the dust-uncorrected Lyman Break Galaxy population (Giavalisco et al. 2004). The SFR density of dust-enshrouded starburst galaxies traced by ultraluminous SHADES galaxies, and completing the luminosity function to lower luminosity galaxies, is estimated to be a factor of 2 larger. This is still a factor of 1.2 to 2 lower than the optical/UV-selected starburst galaxy samples that include the latest dust-correction estimates. The current SHADES survey and complementary multiwavelength data, however, cannot characterize the bulk of the rest-frame FIR emission arising from these lower luminosity galaxies. A more statistically-complete measurement of the universal history of star-formation from powerful dusty, optically-obscured galaxies awaits the commissioning of future large-aperture single-dish and interferometric submillimetre and millimetre telescopes targetting suitable extragalactic fields that have the necessary multi-wavelength ancillary data.

ACKNOWLEDGMENTS

IA and DHH acknowledge partial support from Conacyt grants 39548-F and 39953-F and a Royal Society – Academia Mexicana de Ciencias 2005 exchange program. This work has been also partially funded by PPARC. KC acknowledges additional partial support from NSERC, IRS from the Royal Society, AJB from the Gordon and Betty Moore Foundation, MS from a Gary McCue Fellowship through the Center of Cosmology at UC Irvine, and CS from a PPARC Advanced Fellowship.

REFERENCES

Afonso-Luis A. et al. 2007, in preparation
Almaini O., Dunlop J.S., Conselice C.J., Targett T.A., Mclure R.J., 2005, astro-ph/0511009
Aretxaga I., Hughes D.H., Chapin E.L., Gaztañaga E., Dunlop J.S., Ivison R., 2003, MNRAS, 342, 759
Aretxaga I., Hughes D.H., Dunlop J.S., 2005, MNRAS, 258, 1240.
Aretxaga I., Hughes D.H., Dunlop J.S., 2006, in Baker A.J. et al., eds, From z-Machines to ALMA: (Sub)millimeter Spectroscopy of Galaxies, ASP, in press.
Baugh C., Cole S., Frenk C.S., 1996, MNRAS, 282, 27.
Baugh C. et al., 2005, MNRAS, 356, 1191.
Beasley A.J., Murowinski R. & Tarenghi M., 2006, SPIE, 6267, 2.
Blain A.W., Jameson A., Smail I., Longair M.S., Kneib J.-P., Ivison R.J. et al. 1999, MNRAS, 309, 715
Blain A.W. et al. 2007, in preparation.
Blain A.W., Barnard V.E., Chapman S.C. 2003, MNRAS, 338, 733.
Carilli C.L., Yun M.S., 1999, Ap.J., 513, L13
Carilli C.L., Yun M.S., 2000, Ap.J., 530, 618
Chapman S.C., Smail I., Ivison R.J., Blain A.W., 2002, ApJL, 335, 17
Chapman S.C., Blain A.W., Ivison R.J., Smail I.R., 2003, Nature, 422, 695
Chapman S.C., Blain A.W., Smail I., Ivison R.J., 2005, ApJ, 622, 772
Clements et al., 2007, in preparation.
Condon J.J., 1992, ARAA, 30, 575.
Connolly A.J. et al. 1997, ApJ, 486, L11.
Coppin et al. 2006, MNRAS, 372, 1621.
Dunne L., Clements D.L., Eales S.A., 2000, MNRAS, 319, 813.
Dunlop, J.S. 2005, in de Grijs R., González Delgado R.M., eds, Starbursts: From 30 Doradus to Lyman Break Galaxies, Astrophysics & Space Science Library, Vol. 329, p.121.
Dye S. et al., 2007, in preparation
Greve T.R., Ivison R.J., Bertoldi F., stevens J.A., Dunlop J.S., Lutz D., Carilli C.L., 2004, MNRAS, 254, 779.
Le Floc'h E. et al. 2005, ApJ, 632, 169.
Gaztañaga E. & Hughes D.H., 2001, in Lowenthal J.D., Hughes D.H., eds., Proc. UMass/INAOE Conf., Deep Millimeter Surveys: Implications for Galaxy Formation and Evolution. World Scientific Pub., p. 131.
Giavalisco M. et al. 2004, ApJ, 600, L103.
Granato, G. L., De Zotti, G., Silva, L., Bressan, A. & Danese, L., 2004, ApJ, 600, 580
Greve T.R. et al., 2005, MNRAS, 359, 1165
Heavens A., Panter B., Jiménez R., Dunlop J. 2004, Nature, 428, 625.
Helou G., Soifer T., Rowan-Robinson M., 1985, ApJ, 298, L7.
Holland et al. 1999, MNRAS, 303, 659.
Holland et al. 2006, SPIE, 6275, 45.
Hughes D.H. et al. 1998, Nat, 394, 241.
Hughes D.H. et al. 2002, MNRAS, 335, 871
Hunt L.K., Maiolino R., 2005, ApJL, 626, 15.
Ivison R.J. et al., 2002, MNRAS, 337, 1
Ivison R.J. et al., 2005, MNRAS, 364, 1025
Ivison R.J. et al. 2007, MNRAS, submitted.
Isobe T., Feigelson E.D., Nelson P.I., 1986, ApJ, 306, 490
van Kampen E. 2004, in Plionis M., ed., Multi-Wavelength Cosmology, Kluwer, p. 117
van Kampen E. et al. 2005, MNRAS, 359, 469
Kennicutt, R.C., 1998, ARAA, 36, 189.
Kovács A., Chapman S.C., Dowell C.D., Blain A.W., Ivison R.J., Smail I., Phillips T.G., 2006, ApJ, 650, 592.
Laurent G.T. et al., 2005, ApJ, 623, 742.
Laurent G.T., Glenn J., Egami E., Rieke G.H., Ivison R.J., Yun M.S., Aguirre J.E., Maloney P.R., 2006 ApJ, 643, 1.
Lilly S.J. et al. 1996, ApJ, 460, L1.
Lonsdale C.J et al., 2003, PASP, 115, 897
Mortier A. et al. 2005, MNRAS, 363, 563.
Muanwong O., Thomas P.A., Kay S.T., Pearce F.R., 2002, MNRAS, 336, 527.
Pope A., Borys C., Scott D., Conselice C., Dickinson M., Mobasher B., 2005, MNRAS, 358, 149.
Pope A. et al. 2006, MNRAS, 370, 1185.
Rengarajan T.N., Takeuchi T.T., 2001, PASJ, 53, 433.
Scott S., et al., 2002, MNRAS, 331, 817.
Serjeant S. et al. 2007, in preparation.
Serrano Pérez-Grovas A., Scholerb F.P., Hughes D.H. & Yun M.S., 2006, SPIE, 6267, 1.
Silva, L., De Zotti, G., Granato, G. L., Maiolino, R., & Danese, L., 2005, MNRAS, 357, 1295
Smail I., Ivison R.J., Blain A.W., 1997, ApJL, 490, L5.
Steidel C.C. et al. 1999, ApJ, 519, 1.
Surance J. et al. 2007, in preparation.
Swinbank A.M., 2005, MNRAS, 359, 401
Yun M.S., Carilli C.L., 2002, ApJ, 568, 88.
Yun M.S., Reddy N.A. & Condon J.J., 2001, ApJ, 554, 803.
Wiklind T., 2003, ApJ, 588, 736
Wilson G.W., Austermann J., Logan D.W. & Yun M., 2004, SPIE, 5498, 246

Table 1. Photometric redshifts for SHADES sources in the LH field based on the 1.4GHz/850μm spectral index. The columns give: (1) name of the source; (2) $z^{\rm CY}_{\rm phot}$, photometric redshift using the prescription of Carilli & Yun (1999, 2000); (3) $z^{\rm A}_{\rm phot}$, photometric redshift using the template collection of Aretxaga et al. (2003, 2005), the 90% confidence interval is given in parenthesis; (4) notes on which radio counterpart (from Ivison et al. 2007) is used in the computation of photo-z, in case of ambiguity (N for Northern component, S for Southern component, etc, or 'coadded' if the flux densities from all components are summed); and (5) $z_{\rm spec}$, spectroscopic redshift taken from the literature, where sources for which the redshifts are in parenthesis have reported ambiguities in their radio/optical counterpart associations, or where the redshifts are otherwise under scrutiny. The references for the spec-z (as a superscript of the values) and any debate about them (after the parenthesis, where it applies) are as follows: 1.- Chapman et al. 2005; 2.- Ivison et al. 2005; 3.- Greve et al. 2005; 4.- Chapman et al. 2003; 5.- Swinbank et al. 2005; 6.- Chapman et al. 2002; 7.- Almaini et al. 2005; 8.- Kovács et al. 2006.

object	$z^{\rm CY}_{\rm phot}$	$z^{\rm A}_{\rm phot}$	notes	$z_{\rm spec}$
SHADES J105201+572443 (Lock850.1)	$3.3\pm^{1.8}_{1.2}$	$2.1\pm^{2.0}_{0.1}$ (1.5–6.0)		(2.148[1,2])[2]
SHADES J105257+572105 (Lock850.2)	$5.1\pm^{3.5}_{2.1}$	$3.1\pm^{2.7}_{0.1}$ (2.2–7.0)	SW	
	$6.0\pm^{4.0}_{2.5}$	$3.6\pm^{1.7}_{0.6}$ (2.5–6.9)	NW	
SHADES J105257+572105 (Lock850.3)	$7.0\pm^{4.4}_{3.3}$	$4.1\pm^{1.6}_{0.6}$ (2.7–7.4)	S	(3.036[1])[2]
	$4.2\pm^{2.8}_{1.6}$	$3.1\pm^{1.6}_{0.8}$ (2.0–6.5)	coadded	
SHADES J105204+572658 (Lock850.4)	$3.1\pm^{1.6}_{1.1}$	$2.1\pm^{1.8}_{0.4}$ (1.5–5.8)	coadded	(0.526 or 1.482)[2]
SHADES J105302+571827 (Lock850.5)	$\geqslant 3.8$	$\geqslant 2.9$		
SHADES J105204+572526 (Lock850.6)	$7.3\pm^{4.5}_{3.6}$	$4.1\pm^{1.5}_{0.6}$ (3.0–7.8)		
SHADES J105301+572554 (Lock850.7)	$4.4\pm^{3.0}_{1.8}$	$3.1\pm^{1.8}_{0.6}$ (2.0–6.7)		
SHADES J105153+571839 (Lock850.8)	$\geqslant 3.0$	$\geqslant 2.5$		
SHADES J105216+572504 (Lock850.9)	$3.3\pm^{1.8}_{1.2}$	$2.1\pm^{2.0}_{0.1}$ (1.5–5.9)		1.85[2]
SHADES J105248+573258 (Lock850.10)	$6.4\pm^{0.7}_{2.1}$	$3.4\pm^{2.3}_{0.6}$ (2.2–7.3)		
SHADES J105129+572405 (Lock850.11)	$\geqslant 2.7$	$\geqslant 2.3$		
SHADES J105227+572513 (Lock850.12)	$3.6\pm^{2.2}_{1.5}$	$2.6\pm^{1.7}_{0.6}$ (1.5–6.5)		(2.142[1])[2]
SHADES J105132+573134 (Lock850.13)	$\geqslant 2.6$	$\geqslant 1.5$		
SHADES J105230+572215 (Lock850.14)	$\geqslant 4.0$	$\geqslant 2.2$	no 1.4GHz[a]	2.611[4,2]
SHADES J105319+572110 (Lock850.15)	$3.5\pm^{2.0}_{1.4}$	$2.6\pm^{1.6}_{0.8}$ (1.1–6.0)	coadded	
	$4.6\pm^{3.2}_{2.1}$	$3.1\pm^{1.9}_{0.9}$ (1.7–6.9)	S	
SHADES J105151+572637 (Lock850.16)	$2.3\pm^{1.3}_{0.8}$	$1.6\pm^{1.3}_{0.4}$ (1.0–4.7)		(1.147[1])[2]
SHADES J105158+571800 (Lock850.17)	$2.3\pm^{1.2}_{0.8}$	$1.6\pm^{1.2}_{0.4}$ (1.0–4.2)		2.239[1,2,3,5]
SHADES J105227+572217 (Lock850.18)	$4.5\pm^{3.2}_{1.8}$	$3.1\pm^{2.1}_{0.6}$ (1.5–6.4)		(1.956[1])[4]
SHADES J105235+573119 (Lock850.19)	$\geqslant 2.4$	$\geqslant 1.7$		
SHADES J105256+573038 (Lock850.21)	$\geqslant 2.0$	$\geqslant 1.5$		
SHADES J105137+573323 (Lock850.22)	$\geqslant 2.8$	$\geqslant 2.0$		
SHADES J105213+573154 (Lock850.23)	$\geqslant 2.4$	$\geqslant 1.6$		
SHADES J105200+572038 (Lock850.24)	$3.0\pm^{1.7}_{1.3}$	$2.6\pm^{1.2}_{1.1}$ (1.1–5.8)		
SHADES J105240+572312 (Lock850.26)	$4.3\pm^{3.0}_{2.0}$	$3.1\pm^{1.8}_{1.1}$ (1.5–7.3)		
SHADES J105203+571813 (Lock850.27)	$5.1\pm^{3.5}_{2.3}$	$3.4\pm^{1.6}_{1.1}$ (2.0–6.7)		
SHADES J105257+573107 (Lock850.28)	$\geqslant 2.6$	$\geqslant 2.0$		
SHADES J105130+572036 (Lock850.29)	$\geqslant 2.8$	$\geqslant 2.2$		
SHADES J105207+571906 (Lock850.30)	$1.5\pm^{0.8}_{0.6}$	$1.1\pm^{0.8}_{0.4}$ (0.5–3.2)		2.692[1]
SHADES J105216+571621 (Lock850.31)	$3.7\pm^{2.2}_{1.5}$	$2.6\pm^{1.9}_{0.6}$ (1.5–6.6)		
SHADES J105155+572311 (Lock850.33)	$2.7\pm^{1.3}_{1.1}$	$1.9\pm^{1.2}_{0.6}$ (1.2–5.2)		(3.699[1], 2.686[4,2])
SHADES J105213+573328 (Lock850.34)	$4.9\pm^{0.7}_{0.9}$	$3.4\pm^{1.6}_{1.0}$ (2.0–6.5)		
SHADES J105246+572056 (Lock850.35)	$\geqslant 2.9$	$\geqslant 2.0$		
SHADES J105209+571806 (Lock850.36)	$\geqslant 3.4$	$\geqslant 2.8$		
SHADES J105124+572334 (Lock850.37)	$4.4\pm^{0.9}_{1.4}$	$2.9\pm^{1.6}_{1.1}$ (1.2–6.3)	N ($P=0.013$)	
	$7.1^{1.8}_{1.6}$	$3.9\pm^{2.6}_{1.1}$ (2.0–7.8)	adopted $P=0.078$	
SHADES J105307+572431 (Lock850.38)	$4.2\pm^{2.1}_{1.6}$	$2.4\pm^{1.6}_{1.1}$ (1.2–6.2)		
SHADES J105224+571609 (Lock850.39)	$\geqslant 3.1$	$\geqslant 2.5$		
SHADES J105202+571915 (Lock850.40)	$4.3\pm^{3.1}_{2.0}$	$2.6\pm^{2.0}_{0.6}$ (1.5–6.4)		
SHADES J105159+572423 (Lock850.41)	$2.9\pm^{1.5}_{1.1}$	$2.1\pm^{1.4}_{0.6}$ (1.3–5.3)	S	(0.689[1])[6,2,7,8]
	$2.4\pm^{0.3}_{0.4}$	$1.4\pm^{1.4}_{0.1}$ (1.0–4.7)	N+S	
SHADES J105257+572351 (Lock850.43)	$4.4\pm^{3.2}_{2.1}$	$3.1\pm^{1.9}_{1.1}$ (1.5–7.3)	adopted $P=0.060$	
SHADES J105235+572514 (Lock850.47)	$\geqslant 2.0$	$\geqslant 1.5$		
SHADES J105256+573245 (Lock850.48)	$3.1\pm^{1.1}_{0.6}$	$2.4\pm^{1.6}_{0.9}$ (1.2–6.2)	adopted $P=0.068$	
SHADES J105245+573121 (Lock850.52)	$3.1\pm^{2.0}_{1.4}$	$2.6\pm^{1.6}_{1.1}$ (0.5–5.7)		
SHADES J105240+571928 (Lock850.53)	$\geqslant 2.3$	$\geqslant 1.5$		

[a] This source has a robust 1.4GHz association in the dataset of Ivison et al (2002), but it is below the robustness level adopted for the analysis in this paper, and thus we will make use of the revised 1.4GHz photometry of Ivison et al. (2007) as an upper limit.

Table 1. (cont.)

object	$z_{\rm phot}^{\rm CY}$	$z_{\rm phot}^{\rm A}$	notes	$z_{\rm spec}$
SHADES J105143+572446 (Lock850.60)	$\geqslant 1.4$	$\geqslant 0.8$		
SHADES J105153+572505 (Lock850.63)	$3.9\pm^{2.6}_{1.7}$	$2.6\pm^{2.0}_{0.6}$ (1.5–6.7)		
SHADES J105251+573242 (Lock850.64)	$\geqslant 2.3$	$\geqslant 1.5$		
SHADES J105138+572017 (Lock850.66)	$\geqslant 2.6$	$\geqslant 2.0$		
SHADES J105209+572355 (Lock850.67)	$\geqslant 1.7$	$\geqslant 1.0$		
SHADES J105148+573046 (Lock850.70)	$\geqslant 1.9$	$\geqslant 1.5$		
SHADES J105218+571903 (Lock850.71)	$2.1\pm^{1.1}_{0.8}$	$1.6\pm^{1.1}_{0.6}$ (0.8–4.2)		
SHADES J105141+572217 (Lock850.73)	$3.5\pm^{2.3}_{1.7}$	$2.6\pm^{1.1}_{0.6}$ (1.0–6.2)	N	
	$2.5\pm^{1.5}_{1.0}$	$2.1\pm^{1.1}_{1.1}$ (0.5–5.0)	coadded	
SHADES J105315+572645 (Lock850.75)	$\geqslant 1.2$	$\geqslant 1.1$		
SHADES J105148+572838 (Lock850.76)	$3.0\pm^{1.8}_{1.3}$	$2.1\pm^{1.9}_{0.9}$ (0.8–6.0)		
SHADES J105157+572210 (Lock850.77)	$4.5\pm^{3.1}_{2.4}$	$3.1\pm^{1.0}_{0.6}$ (1.5–7.0)	S	
	$2.4\pm^{0.4}_{0.5}$	$1.9\pm^{1.1}_{0.8}$ (0.8–4.8)	S+N	
SHADES J105145+571738 (Lock850.78)	$\geqslant 1.9$	$\geqslant 1.3$		
SHADES J105152+572127 (Lock850.79)	$3.6\pm^{2.4}_{1.6}$	$2.6\pm^{2.0}_{0.6}$ (1.2–6.5)	adopted $P = 0.064$	
SHADES J105231+571800 (Lock850.81)	$\geqslant 2.2$	$\geqslant 1.9$		
SHADES J105307+572839 (Lock850.83)	$\geqslant 2.1$	$\geqslant 0.8$		
SHADES J105153+571733 (Lock850.87)	$2.1\pm^{1.1}_{0.8}$	$1.6\pm^{1.1}_{0.6}$ (0.5–4.2)		
SHADES J105139+571509 (Lock850.100)	$\geqslant 4.0$	$\geqslant 3.0$		

Table 2. Same as table 1 for SHADES sources in the SXDF field.

object	$z_{\rm phot}^{\rm CY}$	$z_{\rm phot}^{\rm A}$	notes	$z_{\rm spec}$
SHADES J021730-045937 (SXDF850.1)	$4.3\pm^{2.9}_{1.7}$	$3.1\pm^{2.0}_{0.6}$ (2.0–6.8)		
SHADES J021803-045527 (SXDF850.2)	$2.6\pm^{1.4}_{1.0}$	$2.6\pm^{0.7}_{1.1}$ (1.2–5.1)		
SHADES J021742-045628 (SXDF850.3)	$3.3\pm^{1.8}_{1.3}$	$2.1\pm^{1.8}_{0.4}$ (1.5–6.0)		
SHADES J021738-050337 (SXDF850.4)	$1.7\pm^{0.9}_{0.6}$	$1.1\pm^{1.1}_{0.3}$ (0.5–3.5)		
SHADES J021802-050032 (SXDF850.5)	$1.4\pm^{0.6}_{0.5}$	$1.1\pm^{0.6}_{0.5}$ (0.5–2.8)		
SHADES J021729-050326 (SXDF850.6)	$3.1\pm^{0.6}_{0.5}$	$2.4\pm^{1.9}_{0.6}$ (1.3–6.0)	NW	
	$3.6\pm^{1.1}_{1.5}$	$2.9\pm^{1.6}_{1.1}$ (1.6–6.5)	N	
SHADES J021738-050523 (SXDF850.7)	$4.1\pm^{2.8}_{1.7}$	$2.6\pm^{1.9}_{0.6}$ (2.0–7.2)		
SHADES J021744-045554 (SXDF850.8)	$3.3\pm^{1.9}_{1.3}$	$2.6\pm^{1.6}_{0.7}$ (1.2–5.9)		
SHADES J021756-045806 (SXDF850.9)	$\geqslant 2.1$	$\geqslant 1.6$		
SHADES J021825-045557 (SXDF850.10)	$2.3\pm^{1.3}_{0.8}$	$1.6\pm^{1.4}_{0.4}$ (1.0–4.8)		
SHADES J021725-045937 (SXDF850.11)	$2.8\pm^{1.5}_{1.2}$	$2.1\pm^{1.6}_{0.6}$ (1.0–5.6)		
SHADES J021759-050503 (SXDF850.12)	$3.6\pm^{2.2}_{1.5}$	$2.6\pm^{1.7}_{0.9}$ (1.5–6.7)		
SHADES J021819-050244 (SXDF850.14)	$3.4\pm^{2.0}_{1.6}$	$2.6\pm^{1.6}_{1.0}$ (1.2–6.5)		
SHADES J021815-045405 (SXDF850.15)	$\geqslant 2.5$	$\geqslant 2.0$		
SHADES J021813-045741 (SXDF850.16)	$3.5\pm^{2.1}_{1.6}$	$2.6\pm^{1.9}_{0.6}$ (1.5–6.5)		
SHADES J021754-045302 (SXDF850.17)	$\geqslant 2.7$	$\geqslant 2.2$		
SHADES J021757-050029 (SXDF850.18)	$3.9\pm^{2.5}_{1.7}$	$2.6\pm^{2.0}_{0.6}$ (1.5–6.5)		
SHADES J021828-045839 (SXDF850.19)	$2.2\pm^{1.2}_{0.8}$	$1.6\pm^{1.1}_{0.6}$ (0.8–4.6)		
SHADES J021744-050216 (SXDF850.20)	$\geqslant 1.7$	$\geqslant 1.4$		
SHADES J021742-050427 (SXDF850.21)	$0.9\pm^{0.6}_{0.4}$	$0.6\pm^{0.9}_{0.2}$ (0.0–2.2)		
SHADES J021800-050741 (SXDF850.22)	$\geqslant 1.7$	$\geqslant 1.8$		
SHADES J021742-050545 (SXDF850.23)	$2.7\pm^{1.5}_{1.0}$	$2.1\pm^{1.4}_{0.6}$ (1.0–5.0)		
SHADES J021734-050437 (SXDF850.24)	$3.4\pm^{2.0}_{1.7}$	$2.1\pm^{1.8}_{0.6}$ (1.0–6.1)	N	
	$3.7\pm^{2.4}_{1.8}$	$2.6\pm^{2.0}_{0.6}$ (1.5–7.0)	S	
SHADES J021812-050555 (SXDF850.25)	$\geqslant 1.6$	$\geqslant 1.0$		
SHADES J021807-050148 (SXDF850.27)	$1.5\pm^{0.8}_{0.6}$	$1.1\pm^{0.9}_{0.5}$ (0.5–3.3)		
SHADES J021807-045915 (SXDF850.28)	$2.3\pm^{1.3}_{0.9}$	$1.6\pm^{1.4}_{0.6}$ (0.5–4.5)	N	
	$1.7\pm^{1.0}_{0.6}$	$1.1\pm^{1.1}_{0.3}$ (0.2–3.5)	N+S	
SHADES J021816-045511 (SXDF850.29)	$1.6\pm^{0.9}_{0.6}$	$1.1\pm^{0.9}_{0.4}$ (0.6–3.5)		
SHADES J021740-050116 (SXDF850.30)	$4.4\pm^{3.1}_{2.0}$	$3.1\pm^{1.7}_{1.1}$ (1.8–7.7)		
SHADES J021736-045557 (SXDF850.31)	$3.2\pm^{1.8}_{1.3}$	$2.1\pm^{1.6}_{0.6}$ (1.5–6.2)		
SHADES J021722-050038 (SXDF850.32)	$\geqslant 2.1$	$\geqslant 1.5$		
SHADES J021800-045311 (SXDF850.35)	$3.3\pm^{2.0}_{1.5}$	$2.1\pm^{2.1}_{0.5}$ (1.0–6.1)		
SHADES J021832-045947 (SXDF850.36)	$\geqslant 1.9$	$\geqslant 1.8$		
SHADES J021724-045839 (SXDF850.37)	$3.2\pm^{2.0}_{1.5}$	$2.1\pm^{2.1}_{0.5}$ (0.8–6.1)		
SHADES J021825-045714 (SXDF850.38)	$2.7\pm^{1.6}_{1.3}$	$2.1\pm^{1.6}_{0.8}$ (0.5–5.4)		
SHADES J021750-045540 (SXDF850.39)	$\geqslant 1.7$	$\geqslant 1.5$		
SHADES J021729-050059 (SXDF850.40)	$2.9\pm^{1.6}_{1.4}$	$2.1\pm^{2.0}_{0.6}$ (1.0–5.9)		
SHADES J021829-050540 (SXDF850.45)	$\geqslant 4.4$	$\geqslant 3.3$		
SHADES J021733-045857 (SXDF850.47)	$1.5\pm^{0.9}_{0.6}$	$1.1\pm^{0.8}_{0.6}$ (0.2–3.1)	NE	
	$2.6\pm^{1.6}_{1.1}$	$2.1\pm^{1.4}_{1.0}$ (0.6–5.2)	SE	
	$1.3\pm^{0.7}_{0.5}$	$1.1\pm^{0.7}_{0.6}$ (0.2–2.9)	NE+SE	
	$2.2\pm^{1.2}_{1.0}$	$1.6\pm^{1.3}_{0.6}$ (0.5–4.4)	W	
SHADES J021724-045717 (SXDF850.48)	$\geqslant 2.6$	$\geqslant 1.8$		
SHADES J021820-045648 (SXDF850.49)	$\geqslant 1.3$	$\geqslant 1.0$		
SHADES J021802-045645 (SXDF850.50)	$3.6\pm^{2.3}_{1.7}$	$2.1\pm^{2.1}_{0.6}$ (1.2–6.9)		
SHADES J021804-050453 (SXDF850.52)	$2.0\pm^{1.1}_{0.8}$	$1.6\pm^{1.1}_{0.6}$ (0.5–4.1)	E	
	$1.5\pm^{0.9}_{0.6}$	$1.1\pm^{0.9}_{0.6}$ (0.2–3.1)	ES	
SHADES J021752-050446 (SXDF850.55)	$3.0\pm^{1.7}_{1.6}$	$2.1\pm^{2.1}_{0.6}$ (0.8–6.1)		
SHADES J021750-050631 (SXDF850.56)	$\geqslant 1.2$	$\geqslant 0.6$		
SHADES J021745-045750 (SXDF850.63)	$\geqslant 1.6$	$\geqslant 1.5$		
SHADES J021807-050403 (SXDF850.65)	$\geqslant 2.2$	$\geqslant 1.2$		
SHADES J021751-050250 (SXDF850.69)	$\geqslant 1.5$	$\geqslant 1.0$		
SHADES J021811-050247 (SXDF850.70)	$\geqslant 1.9$	$\geqslant 1.2$		
SHADES J021821-045903 (SXDF850.71)	$\geqslant 1.7$	$\geqslant 1.2$		
SHADES J021758-045428 (SXDF850.74)	$2.9\pm^{1.7}_{1.5}$	$2.1\pm^{1.6}_{1.1}$ (0.8–5.8)		
SHADES J021755-050621 (SXDF850.76)	$\geqslant 1.9$	$\geqslant 1.5$		
SHADES J021736-050432 (SXDF850.77)	$2.9\pm^{1.7}_{1.5}$	$2.1\pm^{2.1}_{0.6}$ (1.0–6.1)		
SHADES J021817-050404 (SXDF850.86)	$\geqslant 1.5$	$\geqslant 1.0$		
SHADES J021800-050448 (SXDF850.88)	$\geqslant 1.0$	$\geqslant 1.0$		
SHADES J021734-045723 (SXDF850.91)	$\geqslant 1.5$	$\geqslant 1.2$		
SHADES J021733-045813 (SXDF850.93)	$\geqslant 1.9$	$\geqslant 0.8$		

Table 2. (cont.)

object	$z_{\rm phot}^{\rm CY}$	$z_{\rm phot}^{\rm A}$	notes	$z_{\rm spec}$
SHADES J021740-045817 (SXDF850.94)	$\geqslant 1.5$	$\geqslant 1.2$		
SHADES J021741-045833 (SXDF850.95)	$\geqslant 1.6$	$\geqslant 1.0$		
SHADES J021800-050212 (SXDF850.96)	$3.5\pm^{2.1}_{1.6}$	$3.1\pm^{1.1}_{1.5}$ (1.0–6.3)		
SHADES J021756-045255 (SXDF850.119)	$3.4\pm^{2.0}_{1.6}$	$2.6\pm^{1.7}_{1.1}$ (0.8–6.2)		

Table 3. Photometric redshifts for the sources with additional radio-mm-FIR data reported in the literature from other surveys. The photometry has been complemented at other wavelengths, while preserving the SHADES 450/850μm (Coppin et al. 2006) and 1.4GHz (Ivison et al. 2007) determined flux densities. The first column gives the source-name; the second column gives the most probable mode and error bars based on the 68% confidence interval of the mode calculation (in parenthesis the 90% confidence interval); the third and fourth columns respectively give the bands in which the source is detected at a $\geqslant 3\sigma$ level, and at which upper-limits are used for the computation of the photometric-redshifts; the fifth column provides the published references (and alternative sources-names in overlapping surveys) to the additional photometry, using the following syntax: LE850.x from Scott et al. 2002, 1100.x from Laurent et al. 2005, 2006 and 1200.x from Greve et al. 2004 and Ivison et al. 2005).

object	$z_{\rm phot}$	$\geqslant 3\sigma$ detections	$< 3\sigma$ / upper limits	notes
Lock850.1	$2.4\pm^{1.1}_{0.2}$ (2.2–3.8)	350,850μm,1.1,1.2mm,1.4GHz	175,450μm,3.3mm,5GHz	LE850.1, 1200.5, 1100.14
Lock850.2	$2.9\pm^{0.3}_{0.1}$ (2.5–3.8)	350,850μm, 1.1,1.2mm, 1.4GHz	450μm	LE1100.1, 1200.4, SW-1.4GHz
	$2.9\pm^{0.7}_{0.1}$ (2.8–3.9)			NW-1.4GHz
Lock850.3	$2.9\pm^{0.9}_{0.3}$ (2.5–4.2)	350,850μm, 1.1,1.2mm, 1.4GHz	450μm, 5GHz	LE850.2, 1100.8, 1200.1, S-1.4GHz
	$2.6\pm^{0.3}_{0.1}$ (2.5–3.8)			coadded-1.4GHz
Lock850.4	$1.6\pm^{0.3}_{0.1}$ (1.5–4.8)	850μm, 1.2mm, 1.4GHz	450μm, 5GHz	LE850.14, 1200.3
Lock850.12	$2.6\pm^{0.2}_{0.1}$ (2.2–3.0)	350,850μm, 1.1,1.2mm, 1.4GHz	450μm, 5GHz	LE850.16, 1100.16, 1200.6
Lock850.14	$2.6\pm^{0.8}_{0.1}$ (2.2–3.7)	350,850μm, 1.1,1.2mm	450μm, 1.4,5GHz	LE850.6, 1100.5, 1200.10[a]
Lock850.16	$1.9\pm^{0.4}_{0.1}$ (1.5–3.2)	850μm, 1.2mm,1.4GHz	450μm, 5GHz	LE850.7
Lock850.17	$2.5\pm^{0.6}_{0.5}$ (2.0–5.9)	850μm, 1.2mm, 5,1.4GHz	450μm	LE850.3, 1200.11
Lock850.18	$3.1\pm^{2.9}_{0.1}$ (2.3–6.0)	850μm, 1.2mm, 1.4GHz	450μm	LE1200.9
Lock850.27	$4.6\pm^{1.4}_{0.4}$ (4.0–6.0)	850μm, 1.1,1.2mm, 1.4GHz	450μm, 5GHz	LE1100.4, 1200.7
Lock850.33	$3.6\pm^{0.7}_{0.9}$ (2.4–4.8)	850μm, 1.2mm, 1.4GHz	450μm	LE850.18, 1200.12
Lock850.41	$3.4\pm^{0.7}_{0.2}$ (3.2–4.4)	350,850μm, 1.1,1.2mm, 1.4GHz	450μm	LE850.8, 1100.17, 1200.14
Lock850.76	$4.6\pm^{1.4}_{1.1}$ (3.0–6.0)	850μm,1.1mm,1.4GHz	450μm	LE1100.15

[a] This source has a robust 1.4GHz association in the dataset of Ivison et al (2002), but it is below the robustness level adopted for the analysis in this paper, and thus we will make use of the 1.4GHz photometry of Ivison et al. (2007) as an upper limit.

Table 4. Photometric redshifts for SHADES sources in the LH field based on the 850μm and 1.4GHz data and 450μm upper limits determined by SHADES. The columns give: (1) name of the source; (2) $z_{\rm phot}^{\rm SA}$ survival analysis solution; (3) $z_{\rm phot}^{\rm MC}$ Monte Carlo solution; and (4) notes on associations.

object	$z_{\rm phot}^{\rm SA}$	$z_{\rm phot}^{\rm MC}$	notes
Lock850.1	$2.1\pm^{2.0}_{0.1}$ (1.5–5.9)	$2.4\pm^{0.1}_{0.2}$ (2.0–2.5)	
Lock850.2	$3.1\pm^{2.8}_{0.1}$ (2.4–6.8)	$2.9\pm^{0.6}_{0.1}$ (2.6–3.8)	SW
	$3.6\pm^{2.0}_{0.6}$ (2.5–6.8)	$3.6\pm^{0.4}_{0.4}$ (3.0–4.2)	NW
Lock850.3	$4.1\pm^{2.3}_{0.6}$ (2.8–7.7)	$3.9\pm^{0.6}_{0.4}$ (3.2–4.8)	S
	$3.1\pm^{1.6}_{0.8}$ (2.0–6.1)	$2.6\pm^{0.4}_{0.3}$ (2.2–3.2)	coadded
Lock850.4	$2.1\pm^{1.8}_{0.4}$ (1.5–5.8)	$2.1\pm^{0.3}_{0.1}$ (1.8–3.1)	coadded
Lock850.5	$\geqslant 2.9$	$\geqslant 3.0$	
Lock850.6	$4.1\pm^{2.5}_{0.6}$ (3.0–8.0)	$3.6\pm^{1.0}_{0.1}$ (2.8–4.8)	
Lock850.7	$3.1\pm^{1.8}_{0.6}$ (2.0–6.3)	$2.9\pm^{0.4}_{0.3}$ (2.2–3.4)	
Lock850.8	$\geqslant 2.5$	$\geqslant 2.5$	
Lock850.9	$2.1\pm^{2.0}_{0.1}$ (1.5–5.8)	$2.4\pm^{0.3}_{0.4}$ (2.0–3.2)	
Lock850.10	$3.4\pm^{2.3}_{0.6}$ (2.2–7.0)	$3.1\pm^{0.9}_{0.3}$ (2.8–4.7)	
Lock850.11	$\geqslant 2.2$	$\geqslant 2.5$	
Lock850.12	$2.6\pm^{1.6}_{0.6}$ (1.5–6.2)	$2.6\pm^{0.4}_{0.2}$ (2.2–3.8)	
Lock850.13	$\geqslant 1.5$	$\geqslant 1.5$	
Lock850.14	$\geqslant 2.2$	$\geqslant 2.2$	no 1.4GHz[a]
Lock850.15	$2.6\pm^{1.6}_{0.8}$ (1.2–5.9)	$2.4\pm^{0.4}_{0.4}$ (2.0–3.2)	coadded
	$3.1\pm^{2.0}_{0.9}$ (1.8–6.8)	$2.9\pm^{0.4}_{0.5}$ (2.2–3.8)	S
Lock850.16	$1.6\pm^{1.3}_{0.4}$ (1.0–4.7)	$3.1\pm^{0.1}_{0.7}$ (2.0–3.4)	
Lock850.17	$1.6\pm^{1.2}_{0.4}$ (1.0–4.2)	$2.9\pm^{0.3}_{0.4}$ (2.3–3.2)	
Lock850.18	$3.1\pm^{2.1}_{0.6}$ (1.5–6.1)	$2.9\pm^{0.4}_{0.5}$ (2.2–3.7)	
Lock850.19	$\geqslant 1.8$	$\geqslant 1.5$	
Lock850.21	$\geqslant 1.5$	$\geqslant 1.0$	
Lock850.22	$\geqslant 2.0$	$\geqslant 2.0$	
Lock850.23	$\geqslant 1.6$	$\geqslant 1.5$	
Lock850.24	$2.6\pm^{1.2}_{1.1}$ (1.2–5.8)	$2.4\pm^{0.4}_{0.3}$ (2.0–3.1)	
Lock850.26	$3.1\pm^{1.9}_{1.1}$ (1.5–7.2)	$3.6\pm^{0.1}_{0.8}$ (2.2–3.9)	
Lock850.27	$3.9\pm^{1.9}_{1.1}$ (1.8–6.5)	$3.9\pm^{1.9}_{1.1}$ (1.8–6.5)	
Lock850.28	$\geqslant 2.0$	$\geqslant 2.0$	
Lock850.29	$\geqslant 2.2$	$\geqslant 2.1$	
Lock850.30	$1.1\pm^{0.8}_{0.4}$ (0.5–3.2)	$2.1\pm^{0.1}_{0.4}$ (1.8–2.5)	
Lock850.31	$2.6\pm^{1.9}_{0.6}$ (1.5–6.4)	$2.6\pm^{0.1}_{0.6}$ (2.0–3.1)	
Lock850.33	$2.1\pm^{1.4}_{0.6}$ (1.2–5.4)	$2.1\pm^{0.7}_{0.4}$ (1.8–3.2)	
Lock850.34	$3.4\pm^{1.6}_{1.0}$ (2.0–6.5)	$3.1\pm^{0.6}_{0.2}$ (2.6–3.8)	
Lock850.35	$\geqslant 2.0$	$\geqslant 2.0$	
Lock850.36	$\geqslant 2.5$	$\geqslant 2.5$	
Lock850.37	$2.9\pm^{1.6}_{1.1}$	$4.5\pm^{1.0}_{0.3}$ (4.3–5.8)	N ($P = 0.013$)
	$3.9\pm^{2.6}_{1.1}$	$4.6\pm^{0.6}_{0.1}$ (4.5–5.8)	S (adopted $P = 0.078$)
Lock850.38	$2.6\pm^{1.8}_{1.1}$ (0.8–6.2)	$2.1\pm^{0.1}_{0a.1}$ (2.0–2.3)	
Lock850.39	$\geqslant 2.2$	$\geqslant 2.0$	
Lock850.40	$2.6\pm^{2.2}_{0.6}$ (1.2–6.3)	$2.6\pm^{0.6}_{0.2}$ (2.0–3.2)	
Lock850.41	$2.1\pm^{1.4}_{0.6}$ (1.2–5.3)	$3.6\pm^{0.4}_{0.4}$ (2.5–4.0)	S
	$1.4\pm^{1.4}_{0.1}$ (1.0–4.7)	$2.9\pm^{0.5}_{0.1}$ (2.3–3.5)	N+S
Lock850.43	$3.6\pm^{1.2}_{1.6}$ (1.5–6.6)	$2.4\pm^{0.8}_{0.1}$ (2.2–3.8)	adopted $P = 0.060$
Lock850.47	$\geqslant 1.2$	$\geqslant 1.5$	
Lock850.48	$2.1\pm^{1.5}_{1.1}$ (0.5–5.7)	$2.4\pm^{0.5}_{0.1}$ (2.1–3.0)	adopted $P = 0.068$
Lock850.52	$2.1\pm^{1.9}_{0.6}$ (0.5–5.5)	$2.1\pm^{0.1}_{0.1}$ (1.9–2.2)	
Lock850.53	$\geqslant 1.5$	$\geqslant 1.5$	
Lock850.60	$\geqslant 1.2$	$\geqslant 1.5$	
Lock850.63	$2.6\pm^{2.1}_{0.6}$ (1.5–6.4)	$2.6\pm^{0.4}_{0.4}$ (2.1–3.2)	
Lock850.64	$\geqslant 1.6$	$\geqslant 1.5$	
Lock850.66	$\geqslant 1.5$	$\geqslant 1.5$	
Lock850.67	$\geqslant 1.0$	$\geqslant 1.0$	
Lock850.70	$\geqslant 1.0$	$\geqslant 1.0$	
Lock850.71	$1.6\pm^{1.2}_{0.6}$ (0.5–4.3)	$2.9\pm^{0.1}_{0.7}$ (2.0–3.2)	

[a] This source has a robust 1.4GHz association in the dataset of Ivison et al (2002), but it is below the robustness level adopted for the analysis in this paper, and thus we will make use of the 1.4GHz photometry of Ivison et al. (2007) as an upper limit.

Table 4. (cont.)

object	$z_{\rm phot}^{\rm SA}$	$z_{\rm phot}^{\rm MC}$	notes
Lock850.73	$2.1\pm^{2.6}_{0.2}$ (1.0–6.2)	$2.4\pm^{0.1}_{0.2}$ (2.0–2.5)	N
	$2.1\pm^{1.4}_{0.9}$ (0.7–5.2)	$2.1\pm^{0.1}_{0.1}$ (1.9–2.5)	coadded
Lock850.75	$\geqslant 1.1$	$\geqslant 1.2$	
Lock850.76	$2.1\pm^{1.8}_{0.6}$ (0.8–5.5)	$2.1\pm^{0.2}_{0.1}$ (2.0–2.5)	
Lock850.77	$2.9\pm^{1.7}_{1.1}$ (2.8–6.9)	$2.6\pm^{0.8}_{0.1}$ (2.2–3.8)	S
	$1.5\pm^{1.6}_{0.4}$ (0.8–4.8)	$2.8\pm^{0.4}_{0.4}$ (2.0–3.2)	N+S
Lock850.78	$\geqslant 1.1$	$\geqslant 1.5$	
Lock850.79	$2.6\pm^{2.2}_{0.6}$ (1.2–6.3)	$2.4\pm^{0.6}_{0.1}$ (2.0–3.2)	adopted $P = 0.064$
Lock850.81	$\geqslant 1.9$	$\geqslant 2.0$	
Lock850.83	$\geqslant 0.8$	$\geqslant 1.5$	
Lock850.87	$1.6\pm^{1.0}_{0.6}$ (0.8–4.0)	$2.4\pm^{0.6}_{0.1}$ (1.9–3.0)	
Lock850.100	$\geqslant 2.1$	$\geqslant 2.0$	

Table 5. Photometric redshifts for SHADES sources in the SXDF field based on the 850μm and 1.4GHz data and 450μm upper limits, and when significant, complemented with Spitzer photometry at 70 and 160μm. Columns are as in table 4.

object	$z_{\rm phot}^{\rm SA}$	$z_{\rm phot}^{\rm MC}$	notes
SXDF850.1	$2.9\pm^{2.0}_{0.6}$ (1.8–6.3)	$2.6\pm^{0.4}_{0.3}$ (2.2–3.4)	
SXDF850.2	$2.4\pm^{0.8}_{1.1}$ (1.0–4.8)	$1.9\pm^{0.4}_{0.1}$ (1.8–2.9)	
SXDF850.3	$2.4\pm^{1.5}_{0.6}$ (1.5–5.9)	$2.1\pm^{0.3}_{0.1}$ (2.0–2.6)	
SXDF850.4	$1.1\pm^{1.0}_{0.4}$ (0.5–3.4)	$2.1\pm^{0.4}_{0.2}$ (1.8–2.7)	
SXDF850.5	$1.4\pm^{0.6}_{0.5}$ (0.5–2.8)	$1.4\pm^{0.4}_{0.4}$ (0.6–2.0)	70,160μm included
SXDF850.6	$2.4\pm^{1.9}_{0.6}$ (1.3–6.0)	$2.4\pm^{1.2}_{0.1}$ (2.1–3.8)	NW
	$2.9\pm^{1.6}_{0.9}$ (1.5–6.0)	$2.6\pm^{0.4}_{0.4}$ (2.2–3.7)	N
SXDF850.7	$2.4\pm^{2.1}_{0.5}$ (1.8–6.6)	$2.4\pm^{0.5}_{0.1}$ (2.2–3.4)	
SXDF850.8	$2.4\pm^{1.6}_{0.6}$ (1.2–5.8)	$2.6\pm^{1.3}_{0.1}$ (2.3–4.0)	
SXDF850.9	$\geqslant 1.8$	$\geqslant 1.5$	
SXDF850.10	$1.4\pm^{1.5}_{0.1}$ (0.8–4.6)	$2.6\pm^{0.3}_{0.6}$ (1.9–3.2)	
SXDF850.11	$1.9\pm^{1.5}_{0.6}$ (1.0–5.6)	$2.4\pm^{0.4}_{0.4}$ (2.0–3.4)	
SXDF850.12	$1.9\pm^{2.4}_{0.1}$ (1.2–6.3)	$2.4\pm^{0.3}_{0.4}$ (2.0–3.0)	
SXDF850.14	$2.4\pm^{1.6}_{0.9}$ (1.2–6.3)	$2.4\pm^{0.4}_{0.3}$ (2.0–3.1)	
SXDF850.15	$\geqslant 1.8$	$\geqslant 2.0$	
SXDF850.16	$2.4\pm^{1.9}_{0.6}$ (1.2–6.2)	$2.4\pm^{0.6}_{0.2}$ (2.0–3.2)	
SXDF850.17	$\geqslant 2.0$	$\geqslant 2.0$	
SXDF850.18	$2.4\pm^{2.0}_{0.6}$ (1.5–6.1)	$2.9\pm^{0.2}_{0.6}$ (2.2–3.7)	
SXDF850.19	$1.6\pm^{1.1}_{0.6}$ (0.8–4.6)	$2.4\pm^{0.4}_{0.4}$ (2.0–3.2)	
SXDF850.20	$\geqslant 1.4$	$\geqslant 1.5$	
SXDF850.21	$0.6\pm^{0.9}_{0.2}$ (0.0–2.2)	$0.5\pm^{0.4}_{0.2}$ (0.0–1.2)	70,160μm included
SXDF850.22	$\geqslant 1.8$	$\geqslant 2.0$	
SXDF850.23	$1.9\pm^{1.4}_{0.6}$ (1.0–5.0)	$2.4\pm^{0.9}_{0.2}$ (2.0–3.5)	
SXDF850.24	$2.4\pm^{1.6}_{0.9}$ (1.1–6.0)	$2.4\pm^{0.6}_{0.1}$ (2.2–3.7)	
	$2.9\pm^{1.5}_{1.1}$ (1.5–6.8)	$2.9\pm^{0.1}_{0.6}$ (2.2–3.7)	S
SXDF850.25	$\geqslant 1.0$	$\geqslant 1.0$	
SXDF850.27	$1.1\pm^{0.9}_{0.5}$ (0.5–3.3)	$3.6\pm^{0.1}_{0.8}$ (2.4–3.8)	
SXDF850.28	$1.6\pm^{1.1}_{0.4}$ (0.5–4.4)	$1.4\pm^{0.5}_{0.5}$ (0.6–2.2)	N, 70,160μm included
	$1.2\pm^{1.1}_{0.4}$ (0.2–3.2)	$1.1\pm^{0.4}_{0.1}$ (0.5–1.5)	N+S
SXDF850.29	$1.1\pm^{0.9}_{0.4}$ (0.6–3.5)	$2.1\pm^{0.1}_{0.3}$ (1.8–2.4)	
SXDF850.30	$2.9\pm^{1.8}_{1.1}$ (1.2–6.8)	$2.9\pm^{0.2}_{0.6}$ (2.2–3.8)	
SXDF850.31	$2.1\pm^{1.6}_{0.6}$ (1.5–6.1)	$2.6\pm^{0.5}_{0.4}$ (2.2–3.7)	
SXDF850.32	$\geqslant 1.5$	$\geqslant 1.5$	
SXDF850.35	$2.4\pm^{1.6}_{0.9}$ (1.2–6.2)	$2.4\pm^{0.6}_{0.1}$ (2.1–3.2)	
SXDF850.36	$\geqslant 1.8$	$\geqslant 2.0$	
SXDF850.37	$2.1\pm^{2.1}_{0.5}$ (0.8–5.9)	$2.1\pm^{0.1}_{0.1}$ (2.0–2.4)	
SXDF850.38	$1.9\pm^{1.8}_{0.6}$ (0.3–5.0)	$1.9\pm^{0.2}_{0.1}$ (1.7–2.2)	
SXDF850.39	$\geqslant 1.2$	$\geqslant 1.5$	
SXDF850.40	$2.1\pm^{1.9}_{0.6}$ (1.0–5.8)	$2.4\pm^{0.4}_{0.4}$ (2.0–3.2)	
SXDF850.45	$\geqslant 2.8$	$\geqslant 3.0$	
SXDF850.47	$1.1\pm^{0.8}_{0.6}$ (0.2–3.1)	$1.9\pm^{0.3}_{0.1}$ (1.6–2.2)	NE
	$2.1\pm^{1.4}_{1.0}$ (0.6–5.2)	$2.1\pm^{0.1}_{0.1}$ (1.9–2.2)	SE
	$1.1\pm^{0.7}_{0.6}$ (0.2–2.9)	$1.6\pm^{0.3}_{0.1}$ (1.5–2.1)	NE+SE
	$1.6\pm^{1.3}_{0.6}$ (0.5–4.4)	$2.1\pm^{0.1}_{0.2}$ (1.8–2.4)	W
SXDF850.48	$\geqslant 1.8$	$\geqslant 2.0$	
SXDF850.49	$\geqslant 0.5$	$\geqslant 1.0$	
SXDF850.50	$2.4\pm^{2.0}_{0.9}$ (1.2–6.6)	$2.9\pm^{0.1}_{0.6}$ (2.2–3.6)	
SXDF850.52	$1.6\pm^{1.1}_{0.6}$ (0.5–4.1)	$2.1\pm^{0.1}_{0.2}$ (1.6–2.2)	E
	$1.1\pm^{0.9}_{0.6}$ (0.2–3.1)	$2.1\pm^{0.1}_{0.4}$ (1.5–2.2)	ES
SXDF850.55	$2.4\pm^{1.6}_{1.1}$ (0.5–5.6)	$2.1\pm^{0.1}_{0.2}$ (1.8–2.2)	
SXDF850.56	$\geqslant 0.6$	$\geqslant 1.0$	
SXDF850.63	$\geqslant 1.0$	$\geqslant 1.0$	
SXDF850.65	$\geqslant 1.2$	$\geqslant 1.5$	
SXDF850.69	$\geqslant 0.8$	$\geqslant 1.0$	
SXDF850.70	$\geqslant 1.0$	$\geqslant 1.0$	
SXDF850.71	$\geqslant 0.8$	$\geqslant 1.0$	
SXDF850.74	$2.1\pm^{1.6}_{1.1}$ (0.9–5.8)	$2.1\pm^{0.1}_{0.2}$ (1.8–2.2)	
SXDF850.76	$\geqslant 1.2$	$\geqslant 1.5$	
SXDF850.77	$2.1\pm^{1.0}_{0.6}$ (1.0–6.0)	$2.1\pm^{0.1}_{0.1}$ (1.8–2.2)	$70, 160\mu$m included
SXDF850.86	$\geqslant 1.0$	$\geqslant 1.0$	

Table 5. (cont.)

object	$z_{\rm phot}^{\rm SA}$	$z_{\rm phot}^{\rm MC}$	notes
SXDF850.88	$\geqslant 1.0$	$\geqslant 1.0$	
SXDF850.91	$\geqslant 1.0$	$\geqslant 1.5$	
SXDF850.93	$\geqslant 0.8$	$\geqslant 0.5$	
SXDF850.94	$\geqslant 1.2$	$\geqslant 1.5$	
SXDF850.95	$\geqslant 1.0$	$\geqslant 1.0$	
SXDF850.96	$2.4\pm^{1.8}_{0.9}$ (1.0–6.1)	$2.4\pm^{0.6}_{0.1}$ (2.2–3.5)	
SXDF850.119	$2.2\pm^{1.8}_{1.4}$ (0.0–4.5)	$1.9\pm^{0.1}_{0.5}$ (1.2–2.2)	70,160μm included